

**A VERTICAL AND HORIZONTAL 3-AXIS HAND-HELD CONFOCAL SCANNER
FOR SKIN IMAGING APPLICATIONS**

by
Keqin Chen

B.A.Sc, The University of British Columbia, 2012

A THESIS SUBMITTED IN PARTIAL FULFILLMENT OF
THE REQUIREMENTS FOR THE DEGREE OF

MASTER OF APPLIED SCIENCE

in

THE FACULTY OF GRADUATE AND POSTDOCTORAL STUDIES
(Biomedical Engineering)

THE UNIVERSITY OF BRITISH COLUMBIA
(Vancouver)

April 2015

© Keqin Chen, 2015

Abstract

The goal of this project is to develop a hand-held size, confocal optical scanner for clinical skin imaging. Both vertical and horizontal image scanning have been successfully achieved. Vertical scanning is performed by a voice coil actuator in the Z axial direction and a resonant galvanometer scanner in the X lateral direction. Horizontal scanning is conducted with the same resonant galvanometer scanner and a regular galvo mirror in X and Y lateral directions. The vertical imaging plane is perpendicular to the sample surface, while the horizontal imaging plane is parallel to the sample surface. The developed device is capable of providing image resolutions of 0.9-1.1 μm and 5-8 μm in the lateral and axial directions, respectively. The operational scanning speed is adjustable from 8 to 20 frames per second. Imaging results in both vertical and horizontal directions are presented with biological samples, including onion and mouse skin. By using this hand-held scanner, physicians may be able to reduce the number of unnecessary and repetitive biopsies, which will lower the cost to the health care system.

Preface

The research presented in this thesis was conducted in the University of British Columbia (UBC) MEMS Laboratory in the Department of Mechanical Engineering under the supervision of Dr. Mu Chiao. A portion of research was also conducted in the Imaging Unit of Integrative Oncology Department in the British Columbia Cancer Agency Research Center (BCCRC), under the supervision of Dr. Haishan Zeng.

Table of Contents

| | |
|---|-------------|
| Abstract..... | ii |
| Preface..... | iii |
| Table of Contents | iv |
| List of Tables | vii |
| List of Figures..... | viii |
| List of Symbols | x |
| List of Abbreviations | xi |
| Acknowledgements | xiii |
| Dedication | xiv |
| Chapter 1: Introduction | 1 |
| 1.1 Skin Cancer | 1 |
| 1.2 Current Detection Methods | 2 |
| 1.2.1 Biopsy | 2 |
| 1.2.2 Dermoscope | 2 |
| 1.2.3 Optical Methods for Non-invasive Imaging | 3 |
| 1.2.4 Reflectance Confocal Microscopy | 4 |
| 1.3 Existing Optical Scanners | 5 |
| 1.4 Research Objective | 8 |
| 1.5 Thesis Overview | 9 |
| Chapter 2: Design and Methods | 10 |
| 2.1 Vertical Sectioning..... | 10 |

| | | |
|---------------------|---|-----------|
| 2.1.1 | Lateral X Scan..... | 10 |
| 2.1.2 | Axial Z Scan | 11 |
| 2.2 | Horizontal Sectioning | 13 |
| 2.2.1 | Lateral X Scan..... | 13 |
| 2.2.2 | Lateral Y Scan..... | 14 |
| 2.3 | Three Axis Scanner Assembly..... | 14 |
| 2.4 | System Layout and Overall Assembly..... | 16 |
| 2.5 | Signal Control and Real Time Image Acquisition..... | 20 |
| 2.5.1 | Signal Control | 20 |
| 2.5.2 | Real Time Image Acquisition | 20 |
| Chapter 3: | Results and Discussions..... | 23 |
| 3.1 | System Characteristics | 23 |
| 3.1.1 | Lateral Resolution..... | 23 |
| 3.1.2 | Axial Resolution | 26 |
| 3.1.3 | Voice Coil Performance..... | 27 |
| 3.2 | Imaging Results | 30 |
| 3.2.1 | Vertical X-Z Imaging..... | 31 |
| 3.2.2 | Horizontal X-Y Imaging..... | 34 |
| Chapter 4: | Conclusion and Future Work..... | 38 |
| 4.1 | Summary | 38 |
| 4.2 | Future Work | 41 |
| Bibliography | | 44 |
| Appendices | | 49 |

| | |
|---|----|
| Appendix A Electrical Driver Box Layout for Galvo Mirrors | 49 |
| Appendix B Distortion Correction..... | 51 |
| Appendix C Imaging and Control Labview Software | 54 |
| Appendix D Voice Coil Lens Actuator Assembly Details | 58 |
| Appendix E Operating Procedures for Imaging System..... | 60 |

List of Tables

| | |
|--|----|
| Table 1.1 Comparison of different optical imaging methods | 3 |
| Table 1.2 Disadvantages of various “Real-Time” confocal microscopy scanning mechanisms.... | 7 |
| Table 4.1 Performance comparison of reflectance confocal microscopy systems. | 39 |

List of Figures

| | |
|---|----|
| Figure 1.1 Principle of confocal microscopy [9] | 5 |
| Figure 2.1 Vertical scanning principles | 10 |
| Figure 2.2 (a) Flexure structure to suspend the lens for axial movement (b) Voice coil lens actuator assembly, and part of the three axis scanner (Cross-Sectional View) | 12 |
| Figure 2.3 Relationship between mechanical angle and optical angle in mirror reflection..... | 13 |
| Figure 2.4 Assembly of X, Y, Z scanning actuators in the hand-held device | 15 |
| Figure 2.5 Overall layout of the system, components in yellow area comprise the hand-held portion, the rest of the components are placed on a desktop set-up | 16 |
| Figure 2.6 (a) Physical assembly of the entire system, the desktop components are connected with the hand-held components through optical fibre cable (b) Hand-held portion of the device; 355mL pop can for comparison | 17 |
| Figure 2.7 Skin imaging setup demonstration of the developed hand-held device | 19 |
| Figure 2.8 (a) 1D Line scan without distortion correction (b) 1D line scan image with distortion correction, each line is 25 μ m wide | 21 |
| Figure 3.1 MTF diagram of objective lens A230 with on axis and on edge performances with 300 μ m movement using Zemax Simulation..... | 24 |
| Figure 3.2 (a) Light intensity change of 1D lateral scan on ruled grating (b) Edge responses at different locations | 25 |
| Figure 3.3 FWHM measurement for axial resolution..... | 27 |
| Figure 3.4 (a) Deformation distribution at ~150 μ m displacement and (b) Stress distribution at 150 μ m displacement. Deformation scale for both distributions is 23.67. | 28 |
| Figure 3.5 Peak-Peak voice coil displacement at different driving current..... | 29 |

| | |
|---|----|
| Figure 3.6 Voice coil flexure displacement with driving signal | 30 |
| Figure 3.7 (a) Optical profile image of 50 μ m wide, 100 μ m high, SU-8 deposit on a silicon wafer (b) Vertical cross-sectional 2-D scanning of the same SU-8 deposit, scale bar is 50 μ m | 32 |
| Figure 3.8 (a) Vertical scan of onion epidermis with standard RCM system [28] (b) (c) Vertical scan of onion epidermis with the developed hand-held size system (d) Histology image of onion epidermis, onion sample prepared with Alcian Blue Stain. Image taken using digital microscope | 33 |
| Figure 3.9 Confocal vertical optical section images of onion epidermis from previous developed system[12] | 34 |
| Figure 3.10 (a) Horizontal scan of USAP 1951 resolution target group 7 element 3-6 (b) 10 μ m grid with 1.5 μ m wide line | 35 |
| Figure 3.11 (a) and (b) Horizontal scan of onion epidermis using hand-held scanner c) Onion epidermis under microscope | 36 |
| Figure 3.12 (a) Mouse skin epidermis horizontal confocal image with standard RCM system [28] (b) and (c) Hand-held horizontal scanning confocal image of mouse skin epidermis | 37 |

List of Symbols

| | |
|------------|-----------------------|
| $^{\circ}$ | Degree |
| θ | mechanical tilt angle |
| π | Pi |
| n | refractive index |
| \times | times |
| φ | optical tilt angle |
| λ | Wavelength |

List of Abbreviations

| | |
|---------------|----------------------------------|
| AOD | acousto-optic devices |
| a.u. | arbitrary unit |
| CW | continuous wave |
| DAQ | data acquisition |
| FCM | fluorescence confocal microscopy |
| fps | frames per second |
| μm | micro meter |
| APD | Avalanche photodiode |
| NIR | near infrared |
| PM | polarization maintaining |
| RGS | resonant Galvanometer Scanner |
| DC | direct current |
| MTF | module transfer function |
| FWHM | full width at half maximum |
| Hz | hertz |
| LDV | laser Doppler vibrometer |
| MEMS | micro-electro-mechanical system |
| MPM | multiphoton microscopy |
| nm | nano meter |
| NI | National Instruments |
| NA | numerical aperture |

| | |
|------|---------------------------------|
| P-P | peak to peak |
| RCM | reflectance confocal microscopy |
| RMS | root mean square |
| OCT | optical coherence tomography |
| USAF | US air force |

Acknowledgements

I offer my enduring gratitude to the faculty, staff and my fellow students at UBC, who have inspired me to continue my work in this field. I owe particular thanks to Dr. Mu Chiao and Dr. Haishan Zeng whose penetrating questions taught me to question more deeply. I thank Dr. Harvey Lui for academic support in skin health science, and generous funding through CIHR-Skin Research Training Center scholarship program. I also would like to thank my committee members, Dr. Stella Atkins and Dr. Antony Hodgson for insightful comments to my thesis.

I thank Mr. Hadi Mansoor for enlarging my vision of science and providing coherent answers to my endless questions.

Dedication

Special thanks are owed to my parents and my wife, who have supported me throughout my years of education.

Chapter 1: Introduction

1.1 Skin Cancer

In North America, skin cancer is the most common of all cancers, with over 3.5 million cases being diagnosed each year [1]. If skin cancer is detected late, extensive surgery is necessary, and in the case of malignant melanoma, systemic metastasis and death can occur. At present, skin cancers are detected visually by physicians, but the clinical accuracy of visual diagnoses is inconsistent [2]. The conventional method of diagnosis is to use histological examination of skin biopsies. However, because there is difficulty in locating the exact position of skin cancer and sometimes multiple skin sites are suspicious, many unnecessary biopsies are done, bringing about both considerable cost to the health care system and discomfort to the patient. During skin cancer treatment, visual assessment is also relied upon to determine the amount of tissue to be either excised or irradiated. If a tumor has margins that are poorly defined, it may be necessary to perform repeated biopsy procedures from multiple sites in an expensive and tedious procedure known as Mohs micrographic surgery. Following skin cancer treatment, ongoing patient monitoring by visual inspection and periodic microscopic examination is required for detecting recurrent tumor or de novo skin cancer at other sites. It is clear that all stages in the management of skin cancer would be facilitated by techniques that could provide accurate diagnostic information without multiple expensive and disfiguring skin biopsy procedures. A tool designed specifically for dermatologists to better assess the skin condition non-invasively is in a strong demand, and has shown great market potentials, according to some of the recent developed devices, such as Lucid's VivaScope and Verisante's Auro.

1.2 Current Detection Methods

1.2.1 Biopsy

Skin biopsy is one of the most important diagnostic tests for skin disorders. “Punch biopsy” is considered the primary technique for obtaining diagnostic full-thickness skin specimens. It requires basic general surgical and suture-tying skills. The technique involves the use of a circular blade that is rotated down through the epidermis and dermis, and into the subcutaneous fat, yielding a 3 to 4 mm cylindrical core of tissue sample. Stretching the skin perpendicular to the lines of least skin tension before incision results in an elliptical-shaped wound. Once the specimen is obtained, caution must be used in handling it to avoid crush artifact [3]. After taking biopsy, the tissue sample is fixed and stained and a histology image is usually generated, showing the cross-sectional structure of the skin tissue at different layers. Dermatopathologists will then be able to make diagnosis based on the multi-layer tissue information provided by the cross-sectional histology image.

1.2.2 Dermoscope

The dermoscope is a primary tool for visual inspection and initial diagnosis of skin cancers. A dermoscope is essentially a microscope, and illuminates white light onto the skin surface. Dermatologists can observe magnified skin surface through the magnifying glasses, with the white light reflected from the skin tissue [4]. Light will reflect differently if skin tissue in certain area differentiates from the surrounding area.

1.2.3 Optical Methods for Non-invasive Imaging

Various optical methods have been developed for biomedical imaging applications. The first method is called Optical Coherence Tomography (OCT). OCT is an interferometric imaging technique that maps depth-wise reflections of near-infrared (NIR) light from tissue to form cross sectional images of morphological features at the micrometer scale [5]. The second method is called Reflectance Confocal Microscopy (RCM). RCM relies on the natural variations in refractive indices of tissue microstructures for contrast [6]. The third method is Fluorescence Confocal Microscopy (FCM). FCM makes it possible to obtain high-quality images from exogenous tissue fluorophores, using the fluorescence mode of confocal microscopy [7]. The fourth method is Multi-Photon Microscopy (MPM). MPM uses multi-photon excitation of the fluorophore with near-infrared (NIR) femtosecond laser pulses and high numerical aperture (NA) objectives [8]. Each of these four methods has its own advantages and disadvantages. For comparison, the characteristics of each method are compared in Table 1.1.

Table 1.1 Comparison of different optical imaging methods

| Considerations | OCT | RCM | FCM | MPM |
|--------------------------|-------------------------|-----------------------------|-----------------------------|-------------------------|
| Contrast | Low | High | High | High |
| Resolution | Low(~10 μm) | High(~1 μm) | High(~1 μm) | High(~1 μm) |
| Penetration Depth | Large (~2mm) | Small (~300 μm) | Small (~300 μm) | Medium (~1mm) |
| Speed | High | Medium | Medium | Medium |
| Contrast Agent | No | No | Yes | No |
| Cost | Medium(~50K) | Medium(~50K) | Medium(~50K) | High(~200K) |

For skin tissue imaging, the resolution of OCT is not high enough to observe the detailed tissue structure. The contrast of OCT is also poor due to the speckle effect. On the other hand, FCM requires contrast agent in order to image the tissue. Meanwhile, MPM usually requires an ultra fast pulsed laser source which dramatically increases the cost. Among all the methods, RCM appears to be the most suitable method for optical imaging of skin tissue. It provides a relatively high resolution image, while requiring no contrast agent, and does not require an expensive laser source. The penetration of RCM method is relatively small, but is deep enough to scan the skin epidermis, which usually ranges from 200 μm to 300 μm .

1.2.4 Reflectance Confocal Microscopy

The principle of reflectance confocal microscopy is to detect only the light reflected from the focal point of the scanning sample. There are two pinholes used in reflectance confocal microscopy. One is the pinhole for illumination light that limits the light source spot size, which, in essence, increases the resolution at the focal plane. To obtain a full image, the focal point of light is moved across the specimen by scanning mirrors. Another pinhole is located at the reflected light path so that it rejects any light rays reflected from outside the focal plane, which allows the detector to observe light only from the focal point. A diagram showing the working principle of confocal microscopy is demonstrated below in Figure 1.1.

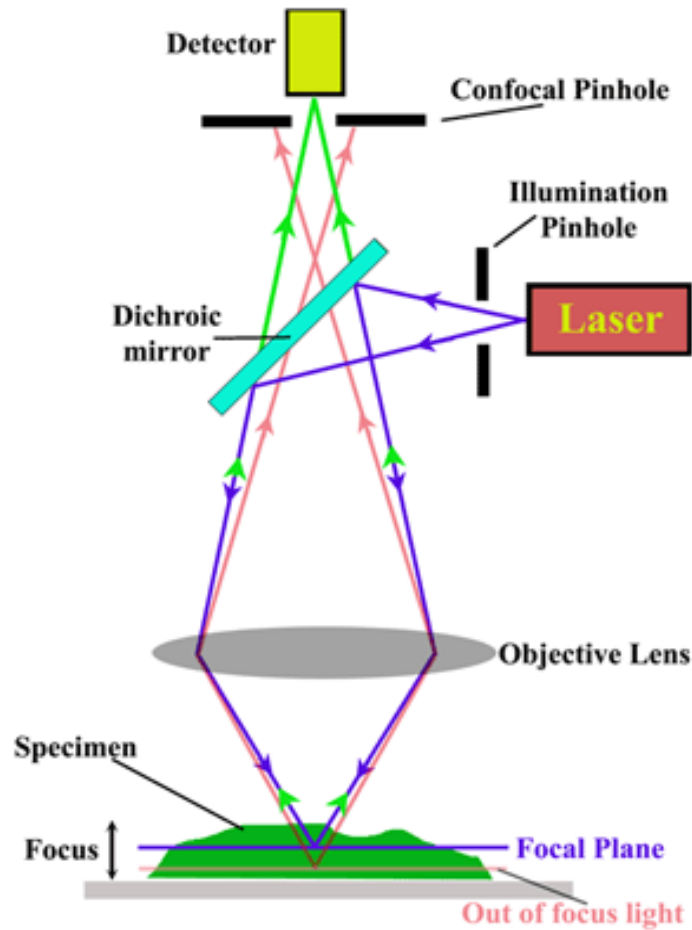


Figure 1.1 Principle of confocal microscopy [9]

1.3 Existing Optical Scanners

Many efforts have been focused on developing confocal microscopy systems to image biological tissues ex-vivo, such as skin [10][11]. It has been shown that, when compared with optical coherence tomography (OCT) the image contrast and resolution of confocal microscopy are of higher quality when viewing tissue and cellular morphology images[12].

Horizontal X-Y plane confocal scanning has been achieved by a variety of methods to tilt light beams using polygon mirrors[10], Galvanometer mirrors[13], Micro-electrical-mechanical-

system (MEMS) mirrors [14]-[17], or actuating an optical fiber [18]. On the other hand, confocal vertical sectioning in the X-Z plane has also been achieved by various methods, such as a piezo translation stage to move the sample specimen in axial Z direction [19][20], or using a piezo actuator in the Z-axis to move the objective lens [21][22]. Some work has been performed to include both horizontal (X-Y) and vertical (X-Z) scanning together into the same scanning system [22][23]. Previously, our research group had successfully presented vertical optical sectioning using a magnetically driven confocal microscanner [12]. The device provided vertical sectioning image that could scan 145 μm range in lateral direction at 2Hz with resolution of 3.87 μm , and 190 μm range in axial direction at resonance (378Hz) with a resolution of 10.68 μm . However, higher resolution and faster imaging speed are desired in order to provide real time detailed tissue structure without any delay in the eyes for a clinical setting.

Fluorescence and reflectance confocal microscopy are the two major techniques being used to provide high contrast and high resolution images. Reflectance confocal microscopy has the advantage of avoiding a contrast agent, which is required in fluorescence confocal microscopy[12]. The absence of using a contrast agent in reflectance confocal microscopy simplifies the clinical procedure, hence enhancing ease of usability. Therefore, we decided to use reflectance confocal microscopy for our system. Fast imaging speed in confocal microscopy is usually desired for physical examinations in order to provide quick feedback on the target being imaged. There are four commonly used methods for real-time confocal microscopy: 1) scanning pinhole disk systems 2) rapid scanning using acousto-optic devices (AOD) 3) slit-scanning systems and 4) scanning using a resonant galvanometer mirror. Each method has its limitations and drawbacks. Table 1.2 summarizes the disadvantages of the corresponding methods [22].

Table 1.2 Disadvantages of various “Real-Time” confocal microscopy scanning mechanisms

| Method | Disadvantages |
|------------------------------|-------------------------------------|
| Scanning Pinhole Disk System | Low light throughput |
| Acousto-optic Devices | Wavelength Dependent |
| Slit-Scanning System | Reduced Confocal Sectioning Ability |
| Resonant Galvanometer | Non-linear sinusoidal scan |

The image distortion caused by the non-linear sinusoidal movement of resonant galvanometers can be corrected to a linearized pattern through software processing [24]. As a result, we choose to use a resonant galvanometer to provide the fast axis scanning speed needed for near real time imaging.

Miniaturizing confocal microscopy system has been an area explored by many research groups, in order to provide a portable hand-held size confocal microscopy system. For example, MEMS techniques have been adopted to fabricate scanning mirrors for scanners that are targeted for endoscopic applications [14]-[16]. However, for external applications such as skin scope, the size of the system does not necessarily need to be as small as would be required on an endoscopic level. The dimension of the hand-held device can be scaled up in order to optimize other aspects of performance. For instance, a larger scanning mirror will allow larger optics to be used so that the image quality can be improved. As long as the overall size of the device is still portable for hand-held use, the dimensions of optical components are not primary constraints in

the design criteria. Therefore, the target size of the device is determined to be comparable with a pop can.

Recently, there is a commercially available RCM based device, VivaScope, developed by Caliber ID (previously Lucid Inc.). It provides reflectance confocal imaging in the horizontal plane that is parallel to the skin surface, at cost of \$50000-60000 for a hand-held size device. Although it is helpful to provide horizontal image, it is difficult to determine the depth of scanning for the horizontal image. Estimation of the vertical distance is challenging with horizontal scanning image. This challenge brings the necessity of vertical scanning to show cross-sectional image of different depth.

1.4 Research Objective

Based on the experiences from our previous vertical sectioning device, high resolution and fast imaging speed are desired in order to provide real time detailed tissue structure in a clinical setting. Meanwhile, in order to have scanning in both horizontal and vertical imaging, faster scanning speed in X direction and slower scanning with controllable vibration in Z direction are desired. Our previous electromagnetic driven actuator in Z direction could only vibrate at resonant frequency, which was about 300Hz. Nevertheless, a compact and portable assembly of the scanning system is also desired so that imaging can be performed with more accessibility and convenience on different body locations, such as neck, legs or torso.

The research hypothesis is that a hand-held optical skin scanner using a non-invasive method to image vertical sectioning of the skin tissue in real time is achievable and can be developed.

The objective for this project is to develop a hand-held size probe that can scan tissue in a $200 \times 200 \mu\text{m}^2$ cross-sectional area perpendicular to the skin surface with high scanning resolution and speed. The image obtained from the scanning needs to provide enough details with high quality resolution of $1 \times 5 \mu\text{m}$ for skin cancer diagnosis, and the scanning speed of this device needs to be high enough (>10 frames per second (fps)) for fast imaging.

1.5 Thesis Overview

This thesis is organized by the introduction in chapter 1, followed by chapter 2 and chapter 3 with design, methods, results and discussions, then ends with chapter 4, final conclusions and discussion of future work.

Chapter 1 introduces the need for a non-invasive optical method for skin cancer detection and provides an overview of the state-of-the-art methods in optical imaging.

Chapter 2 describes the hardware and software design and methods used to construct the imaging system.

Chapter 3 presents the results obtained using the developed imaging system, including the system characteristics and various imaging results.

Chapter 4 summarizes the work that has been completed and discusses the future potentials with the developed imaging system.

Chapter 2: Design and Methods

2.1 Vertical Sectioning

As shown in Figure 2.1, there are two scan directions in the vertical cross-sectional scanning, the lateral (X-axis) direction, and the axial (Z-axis) direction. A raster scanning pattern across the imaging area is generated by the linear movement of focal point in both lateral and axial directions. The vertical scanning image plane is perpendicular to the sample surface.

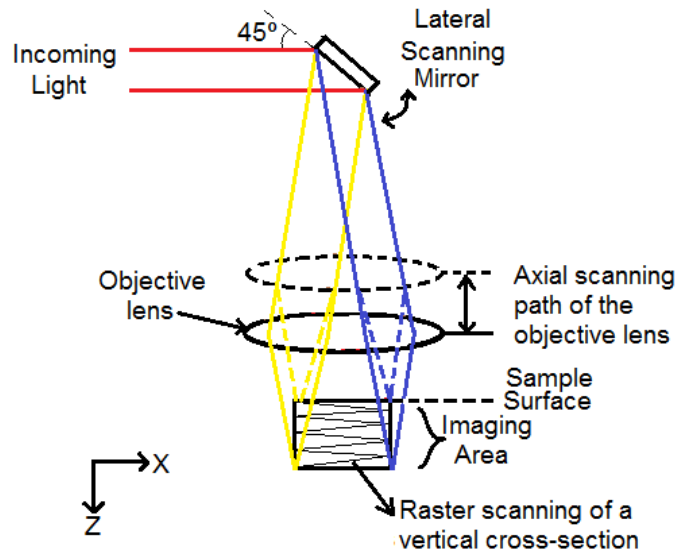


Figure 2.1 Vertical scanning principles

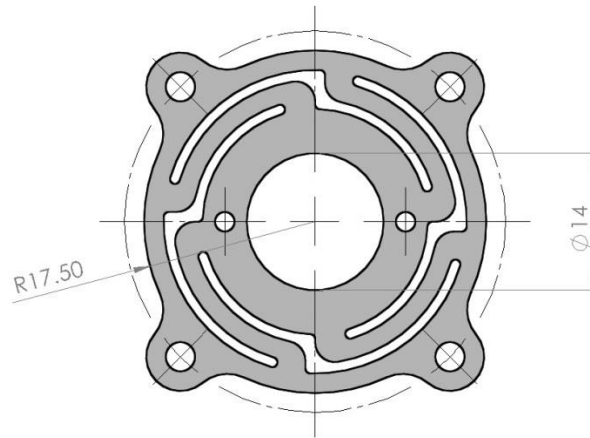
2.1.1 Lateral X Scan

The scanning movement in the lateral direction is achieved by using an off-the-shelf resonant GS (Galvanometer scanner, Cambridge Technology 4KHz CRS). The resonant GS has a resonant motor with a silver coated reflective mirror attached that can tilt sinusoidally at different angles under different driving voltages. By inputting a constant DC driving voltage (0~5V) to the

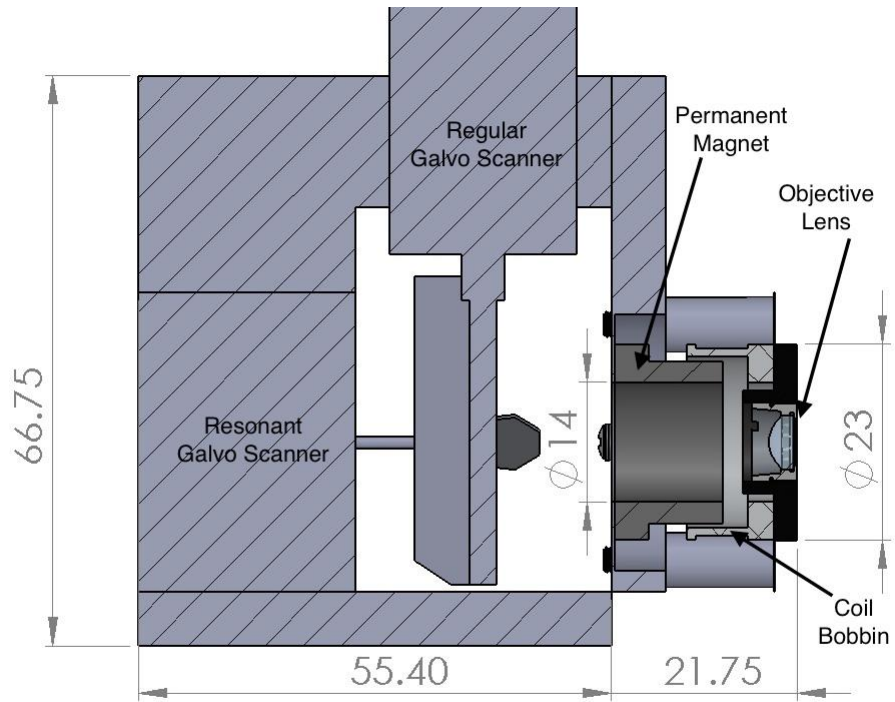
resonant GS, the mirror surface can be controlled to start rotating back and forth at a certain angle (maximum 20 °). The rotation of the resonant GS mirror surface causes the incoming light beam to be reflected at different angles, hence, forming a linear scanning pattern at a distal plane. The frequency of the rotation is fixed at its resonance, 3920Hz, in the current resonant GS. The optical clear aperture diameter of the resonant GS mirror is 12mm, resulting a 8.48mm effective beam diameter when the mirror is placed at 45 °, as shown in Figure 2.1.

2.1.2 Axial Z Scan

The scanning movement in the axial direction is achieved by using an electromagnetic voice coil (NCC01-09-001-1NH, H2W Technologies). Voice coil is a type of linear motor, originally used in amplifiers. It consists of a permanent magnet field and a coil winding (conductor) to produce a force proportional to the current applied to the coil [25]. The linear motion is controlled by the driving signal in the coil. This linear voice coil actuator is designed with a 14mm hole in the center, which allows room to place the objective lens. The voice coil contains two parts, a ring-shaped permanent magnet and a coil bobbin. In our application, the ring-shaped permanent magnet is fixed onto holder, and the voice coil bobbin is attached to the objective focal lens through a non-magnetic flexure structure (Figure 2.2 (a)), fabricated using a waterjet cutter with 0.2mm thick stainless steel 304 sheet. The flexure structure acts as a spring to allow periodical movement of the voice coil. This movement causes the scanning in the axial direction, which results in the focal point to move at different focal depths. The symmetrical beam pattern on the flexure allows equal displacement in the axial direction and prevents the lens from tilting during actuation. Figure 2.2 (b) shows the cross-sectional view of the voice coil actuator assembly. Detailed voice coil actuator assembly is shown in Appendix D .



a)



b)

Figure 2.2 (a) Flexure structure to suspend the lens for axial movement (b) Voice coil lens actuator assembly, and part of the three axis scanner (Cross-Sectional View)

2.2 Horizontal Sectioning

Horizontal scan is performed by operating lateral scanning in the X and Y directions using the 4KHz resonant GS and a regular galvanometer scanner (regular GS) with a 15mm aperture silver coated mirror (Cambridge Technology, 6231H). The reason to use galvo mirrors for both lateral scanning direction is to maximize optical beam size comparing to MEMS mirrors, but also to minimize the overall physical size comparing to polygon mirrors.

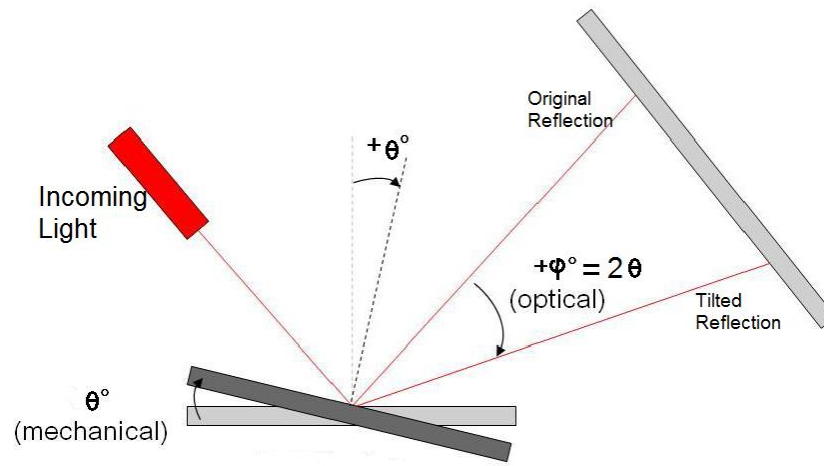


Figure 2.3 Relationship between mechanical angle and optical angle in mirror reflection

2.2.1 Lateral X Scan

The lateral X Scan of horizontal scanning uses the same resonant GS as vertical scanning, operating at fast scanning speed of 3920Hz. The relationship between the mechanical and optical angles during lateral scanning is shown in Figure 2.3. The incoming light is reflected by a tilting mirror to achieve a line scan at a remote surface. The mechanical tilting angle θ of the mirror is half of the reflected light angle ϕ , due to the doubling effect of the mirror surface.

2.2.2 Lateral Y Scan

Lateral Y Scan is achieved by using a regular galvanometer scanner. The regular GS is controlled by a servo driver (Cambridge technology, the MicroMax Model 671XX), and is operated at the desired slow scanning frequency, typically 10Hz in the developed system. The scanning principle is similar to the scanning principle in the X direction. The regular GS can be controlled with different analog signal waveforms, such as Saw tooth, Square, Sinusoidal, or Angular waveforms. The movement and amplitude of the scanning mirror will follow the type and magnitude of the input driving signal.

2.3 Three Axis Scanner Assembly

The hand-held scanner is assembled with three actuators for three axis scanning. As shown in Figure 2.4, the incoming light is first reflected by the resonant GS placed at 45° in the X-axis, and is then reflected by the regular GS placed at 45° in the Y-axis. The light then passes through the voice coil actuated objective lens.

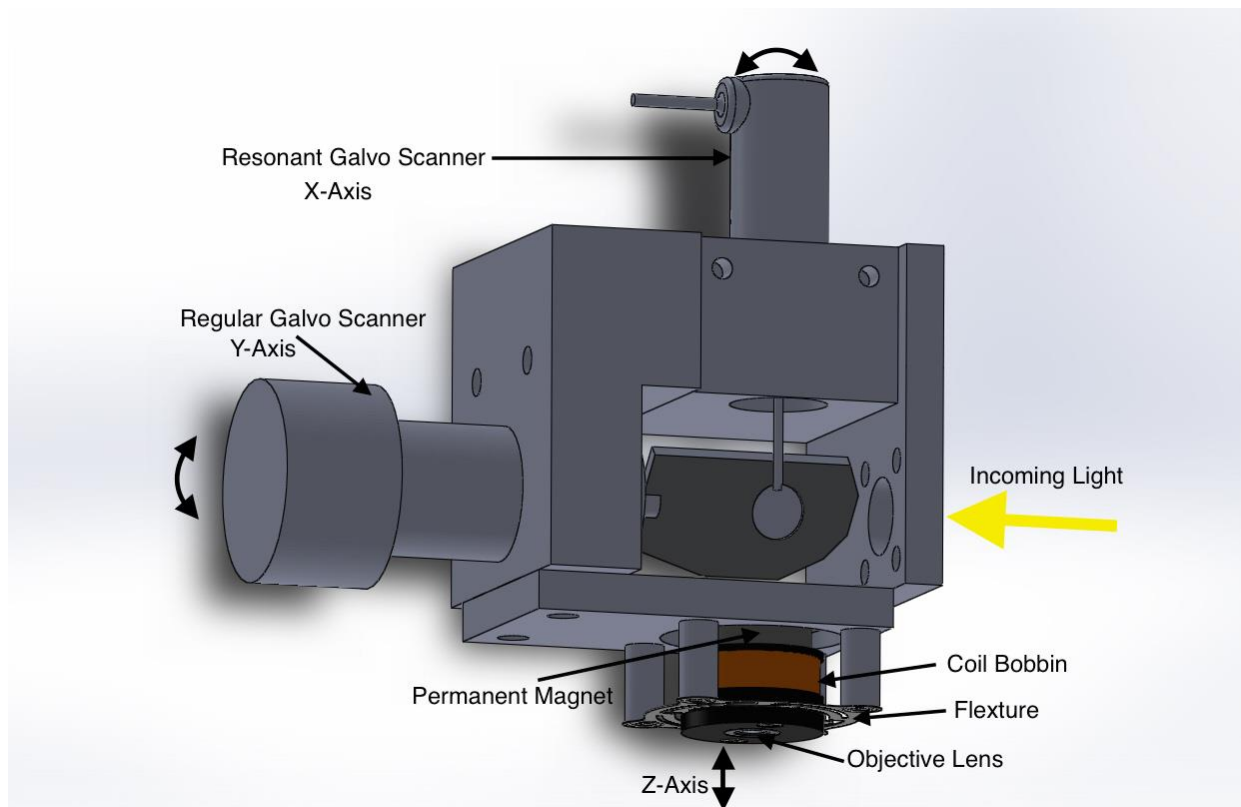


Figure 2.4 Assembly of X, Y, Z scanning actuators in the hand-held device

2.4 System Layout and Overall Assembly

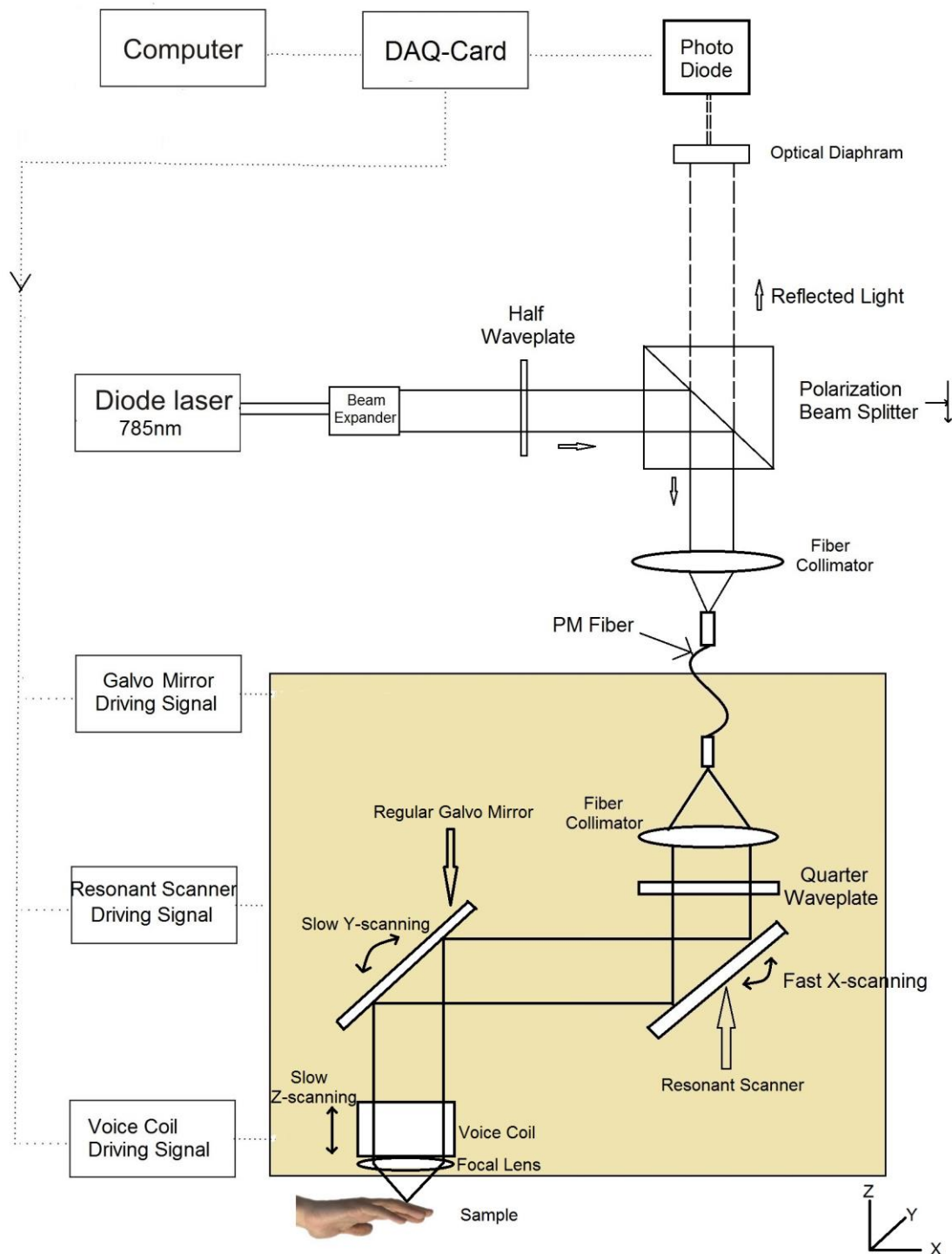


Figure 2.5 Overall layout of the system, components in yellow area comprise the hand-held portion, the rest of the components are placed on a desktop set-up

Figure 2.5 shows the overall layout of the design, including both the hand-held device and desktop setup. The components within the yellow background comprise the hand-held portion of the device. Figure 2.6 a) shows the physical assembly of the entire system. The desktop part and hand-held part are connected through the blue jacket optical fiber. Figure 2.6 b) shows the hand-held part of the scanner in comparison with a pop can. The resonant scanner and galvo mirror have electrical wires connected to the electrical control box for power and signal control.

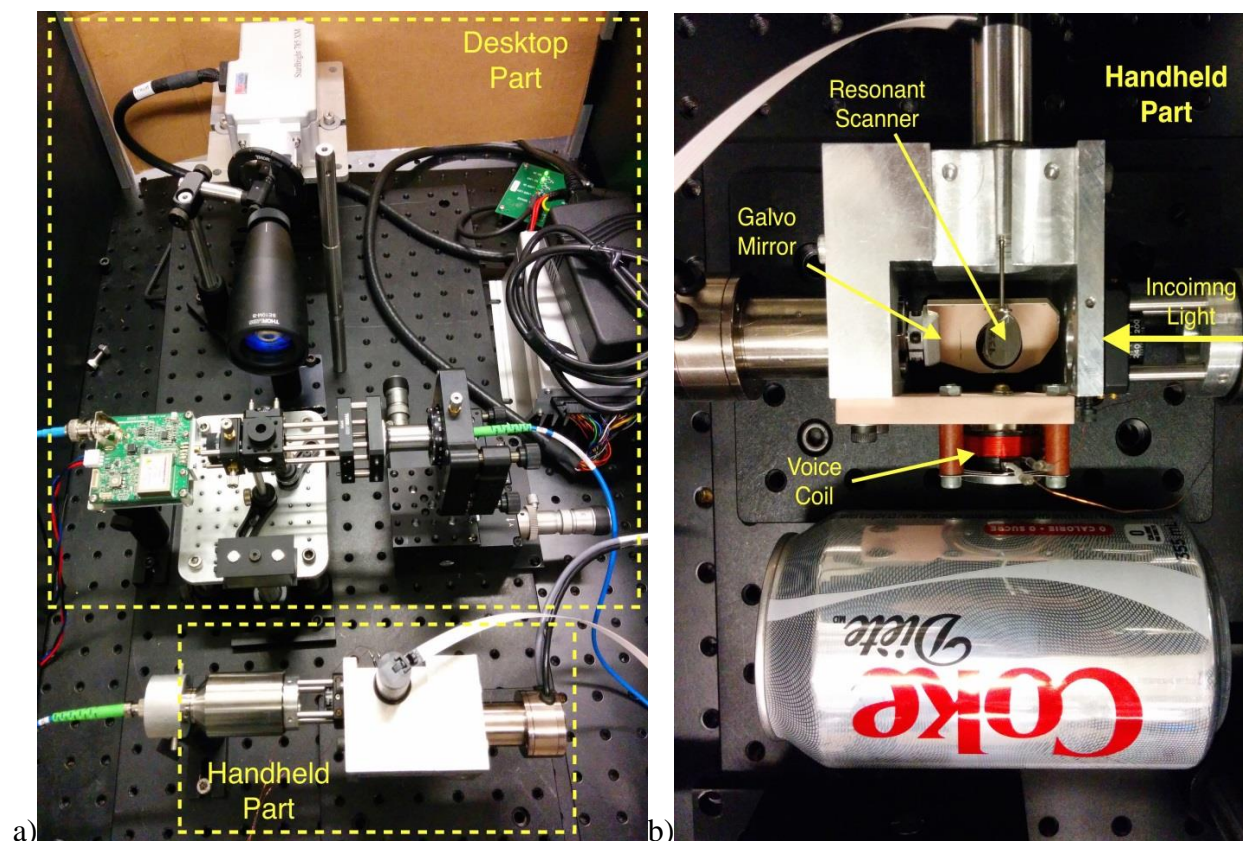


Figure 2.6 (a) Physical assembly of the entire system, the desktop components are connected with the hand-held components through optical fibre cable (b) Hand-held portion of the device; 355mL pop can for comparison

In the desktop setup, we use a single wavelength 785 nm near-infrared laser diode (Starbright 785 XM, Torsana Laser Technologies) to generate a polarized laser beam with 500mW power as our light source. The 785nm wavelength is selected in order to achieve enough tissue penetration for biological samples, and sufficient photonic energy for light scattering. The light is controlled with reduced power by placing a metallic neutral density filter in front of the laser source. The controlled light first passes through a 10X beam expander to expand the beam size from 1mm to approximately 10mm. The expanded light then passes through a half-wave plate, which aligns the polarization of the light with the Polarizing Beam Splitter so that the maximum amount of light is reflected. This results in only the vertical polarized light being reflected. A small amount of non-vertical polarized light passes directly through the beam splitter, and is absorbed by a light stopper. The reflected light passes through a fiber coupling objective lens (Newport M-10X), which focuses the light into a single mode polarization maintaining fiber with 4 μ m mode field diameter (Thorlabs HB750). The fiber in this design acts as the confocal pinhole for both incoming and reflected light. The fiber also acts as the connecting cable between the desktop setup and the hand-held device.

In the hand-held device, the light coming out of the fiber is collimated into a 15mm diameter beam using a fiber collimator (Silicon Lightwave Technology LB20R-780P-F2). The collimated light then passes a quarter-wave-plate. The quarter-wave-plate changes the linear polarized light to a circular polarized light before it hits the Galvanometer mirror. After the Galvanometer mirror reflection, the light is finally focused onto the sample by a commercially available focal lens with NA of 0.55 and 5mm clear aperture (Thorlabs A230TM-B).

The single scattered light reflected back from the sample follows the same path as incoming light. All the lights reflected not from the focal point are rejected by the single mode fiber (acting as the confocal pinhole). However, because the reflected light passes the quarter-wave-plate again, the polarization of the reflected light is rotated by another 45 degrees. This will change the vertical polarized incoming light into a horizontal polarized reflected light, and allow the reflected light to pass directly through the beam splitter and be detected by the avalanche photo diode (HAMAMATSU C10508).

A Data Acquisition Card (DAQ-Card) is used to generate the driving signals for the resonant scanner, the Galvanometer mirror, as well as the voice coil. At the same time, the DAQ-Card records the light signals from the photo diode.

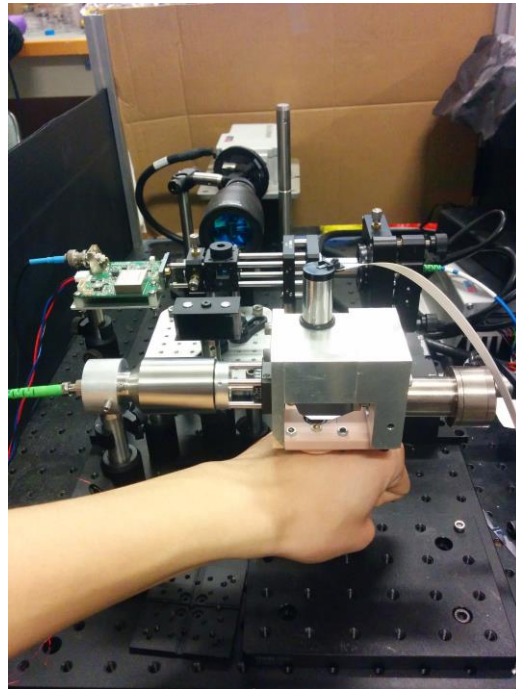


Figure 2.7 Skin imaging setup demonstration of the developed hand-held device

Figure 2.7 demonstrates the orientation and setup for skin imaging. Proper mechanical mounting and optical interface are still needed to be designed for stable and high quality imaging on the skin surface. Imaging gel or liquid may be required.

2.5 Signal Control and Real Time Image Acquisition

2.5.1 Signal Control

A control and image recording program in Labview was developed to drive the resonant scanner, the galvo mirror, and the voice coil, as well as to record real time image. The driving signals are generated using a Data Acquisition Card(NI-DAQ USB 6335). The reflected light signal from an imaging sample is detected by the photo diode, which converts light signals into electrical signals for the Data Acquisition Card to read. A real time image is constructed in the Labview program to display the vertical scanning area. Gray scale image is generated based on the reflected light intensities at different positions within the scanning area.

The driving signals for regular galvo mirror and voice coil are synchronized with the sync signal from the resonant scanner. This will allow all the driving signals to start at the same time and avoid phase shifts between different scanning directions.

2.5.2 Real Time Image Acquisition

The original acquired image signals contain distortion due to the sinusoidal movement of actuators [26][31]. Without image processing, the original image recorded would show a magnified sample around the edge, while features at center are compressed, as shown in figure 7. A real time distortion correction method for image linearization [24] is embedded in the Labview image recording software to correct the image distortion. Detailed code used in the Labview

program is shown in Appendix B . The C++ code is implemented into the Labview program through a "call library function node" as a .dll file.

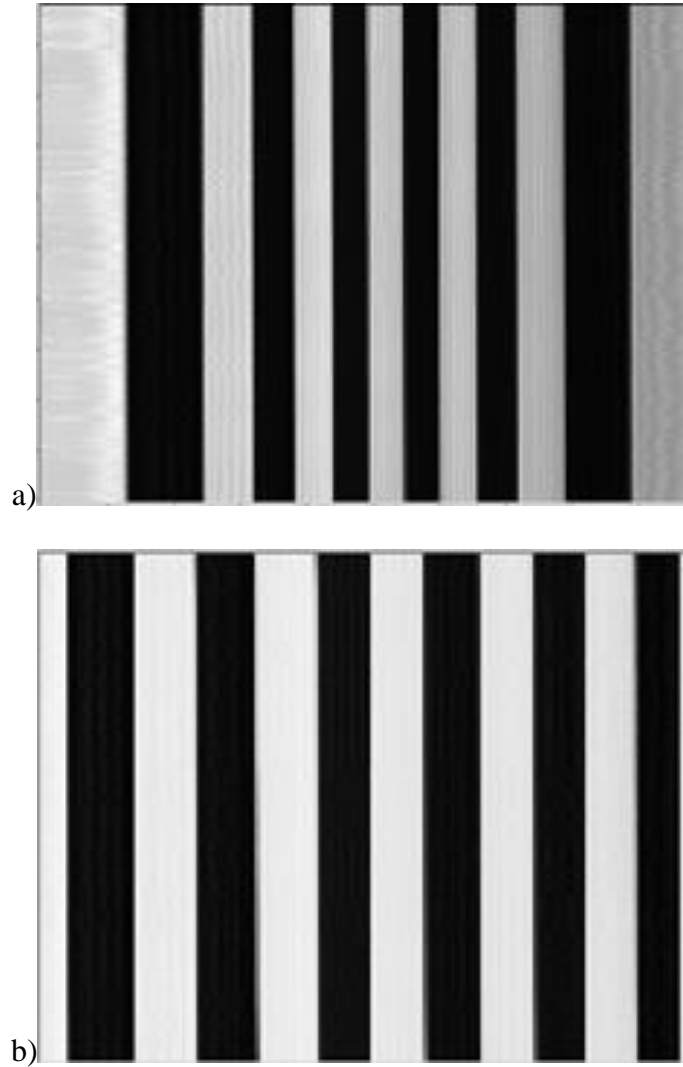


Figure 2.8 (a) 1D Line scan without distortion correction (b) 1D line scan image with distortion correction, each line is 25 μ m wide

Figure 2.6 shows the effect of distortion correction on the original image. The 1D line being scanned is 20LP/mm grating. Each line has equal widths of 25 μ m. Figure 2.8 (a) shows the

distortion effect of sinusoidal movement, causing the line at the edge of the image to be falsely enlarged, while in contrast, the lines in center of the image are compressed. Figure 2.8 (b) shows lines of equal width across the entire image after performing real time software correction in image linearization.

Chapter 3: Results and Discussions

3.1 System Characteristics

3.1.1 Lateral Resolution

The theoretical lateral resolution is calculated to be $0.73\text{ }\mu\text{m}$, using the following equation [27]:

$$R_{lateral} = \frac{0.51 \times \lambda}{NA} \quad (1)$$

where λ is the light wavelength, 785nm , and NA is the numerical aperture of the objective lens, 0.55 .

Software simulation of the objective lens using Zemax suggests the lateral resolution at center to be $0.93\text{ }\mu\text{m}$ and at edge to be $1.20\text{ }\mu\text{m}$, based on the spatial frequency of 535 and 415 at 10% on the Module Transfer Function (MTF) diagram (Figure 3.1).

Experimentally, we verified the lateral resolution by scanning across a series of ruled gratings along the X direction using a variable frequency target (Edmund Optics DA002E). The lateral resolution is defined using edge response method (Figure 3.2 (a)). For a Gaussian spot, the lateral resolution can be defined as 0.78 times the distance changing from 10% to 90% of maximum light intensity when scanning across a sharp edge [10]. The resulting average lateral resolution is about $0.9 - 1.1\text{ }\mu\text{m}$ (Figure 3.2 (b)).

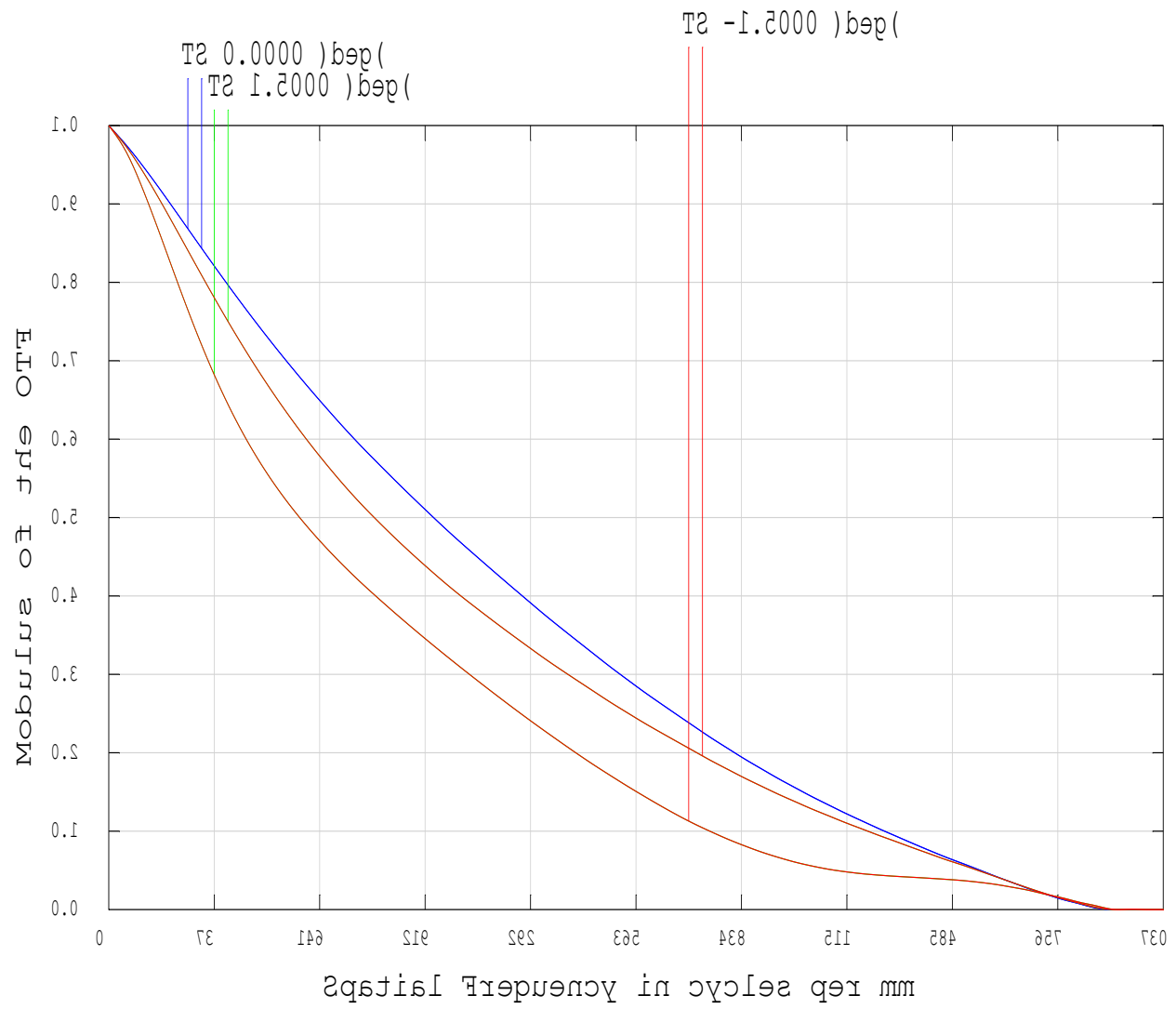
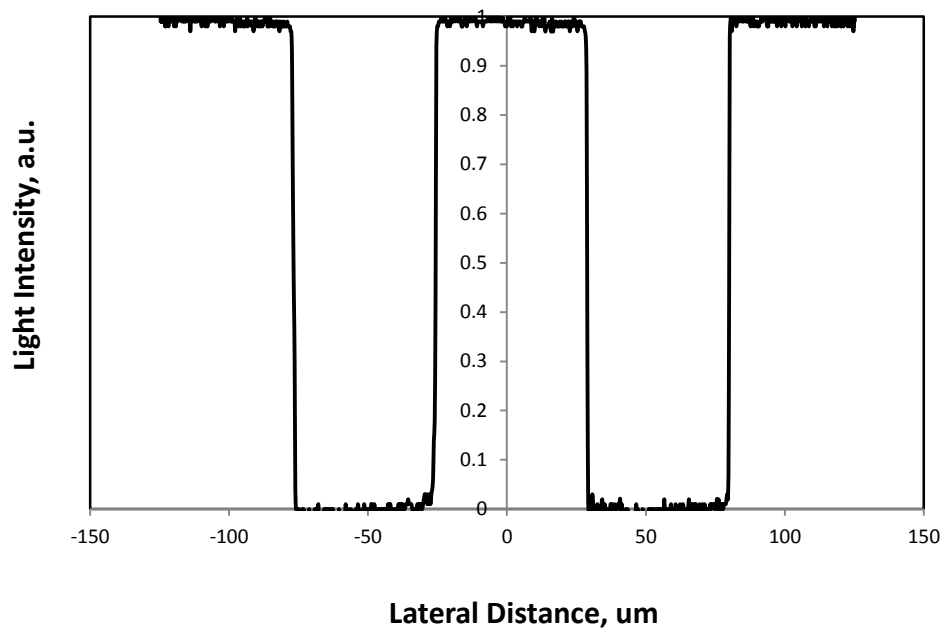
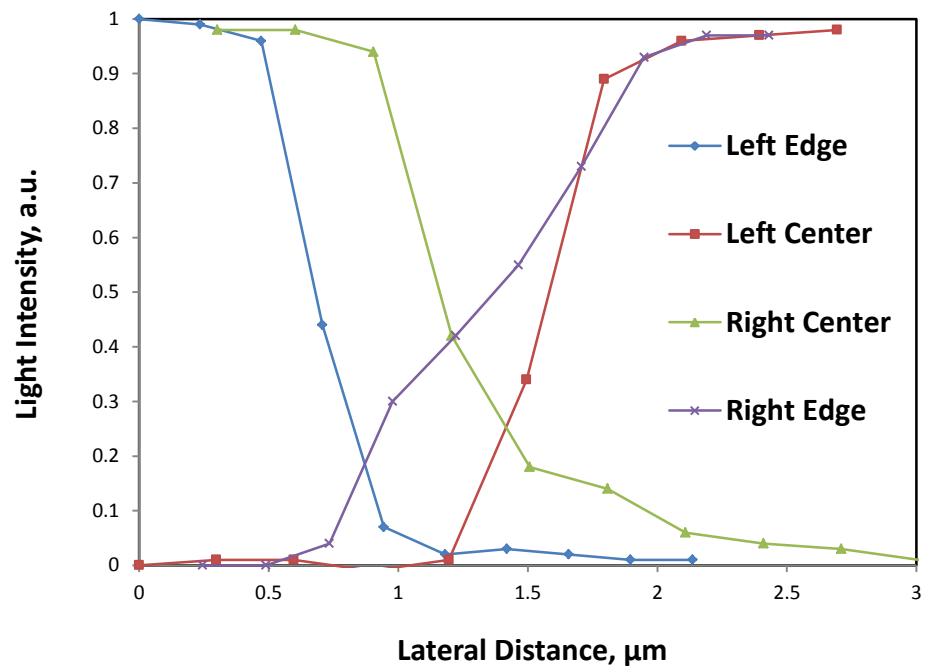


Figure 3.1 MTF diagram of objective lens A230 with on axis and on edge performances with 300 μm movement using Zemax Simulation



a)



b)

Figure 3.2 (a) Light intensity change of 1D lateral scan on ruled grating (b) Edge responses at different locations

3.1.2 Axial Resolution

The theoretical axial resolution is calculated to be 4.2 μm , using the following equation when pinhole size is large [27]:

$$R_{axial} = \frac{0.88 \times \lambda}{n - \sqrt{(n^2 - NA^2)}} \quad (2)$$

where λ is the wavelength of the laser, 785nm. n is the refractive index of air, 1. NA is the numeric aperture of the focal length, 0.55.

The axial resolution is experimentally evaluated by scanning across a reflective mirror in the Z direction and recording the change in light intensity. A peak intensity will appear when the focal plane coincides with the reflective mirror surface. Using the Full Width at Half Maximum (FWHM) method, the width of half maximum represents the axial resolution, about 5-8 μm . Figure 3.3 shows how light intensity varies across the focal point in the axial direction.

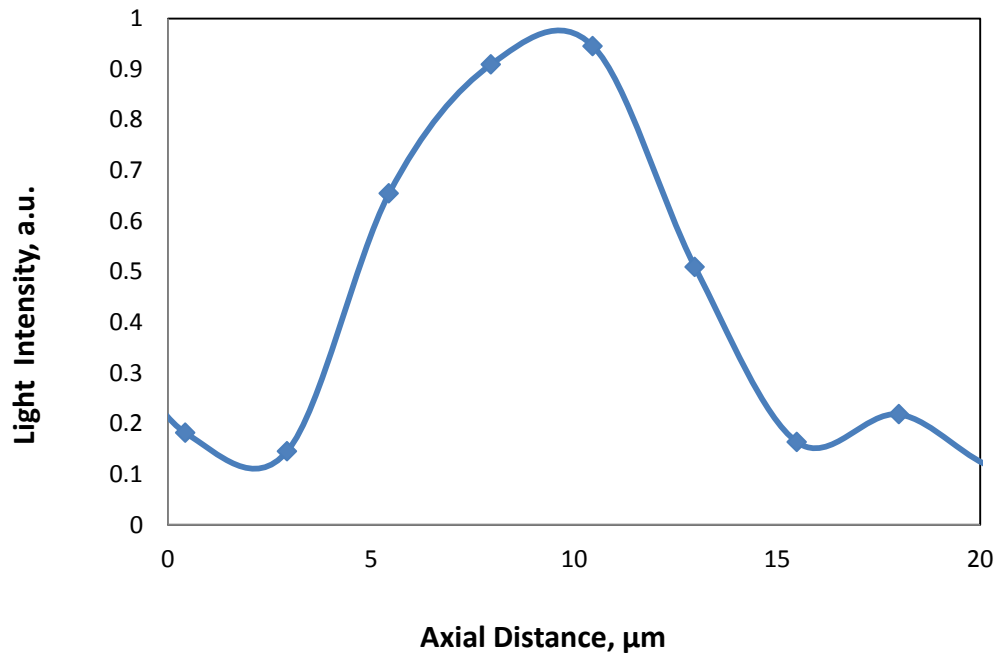


Figure 3.3 FWHM measurement for axial resolution

3.1.3 Voice Coil Performance

In order to achieve a scanning range totally $300\mu\text{m}$, the voice coil moves with a $150\mu\text{m}$ displacement on each side. A deformation and stress distribution analysis are performed using Solidworks SimulationXpress, shown in Figure 3.4 (a) and (b). The lowest factor of safety when moving at $150\mu\text{m}$ is 2.02 in our design.

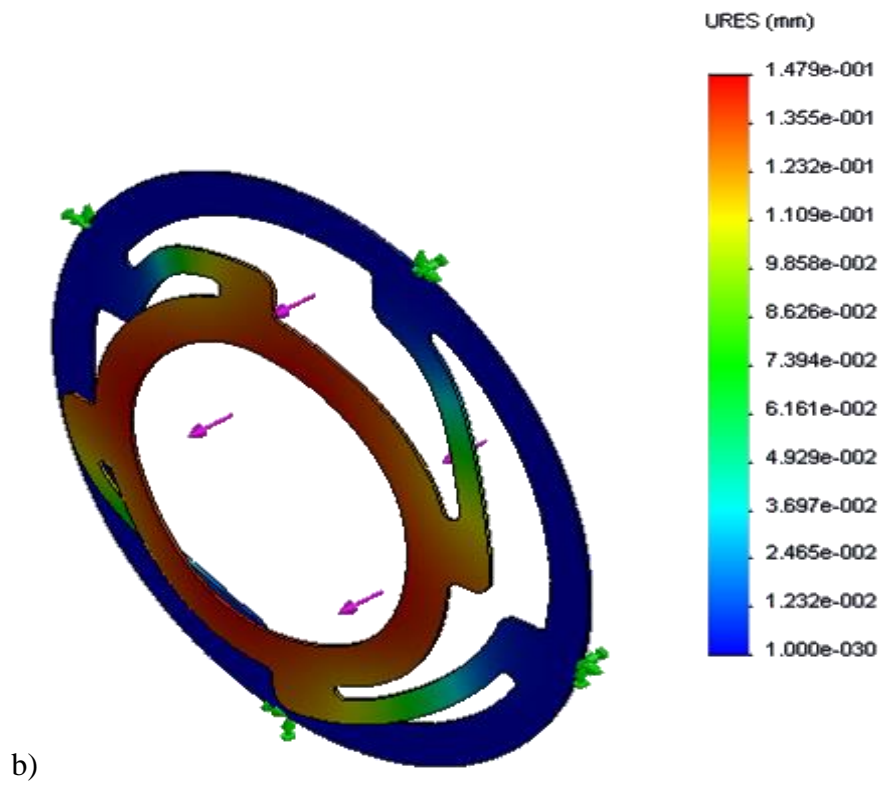
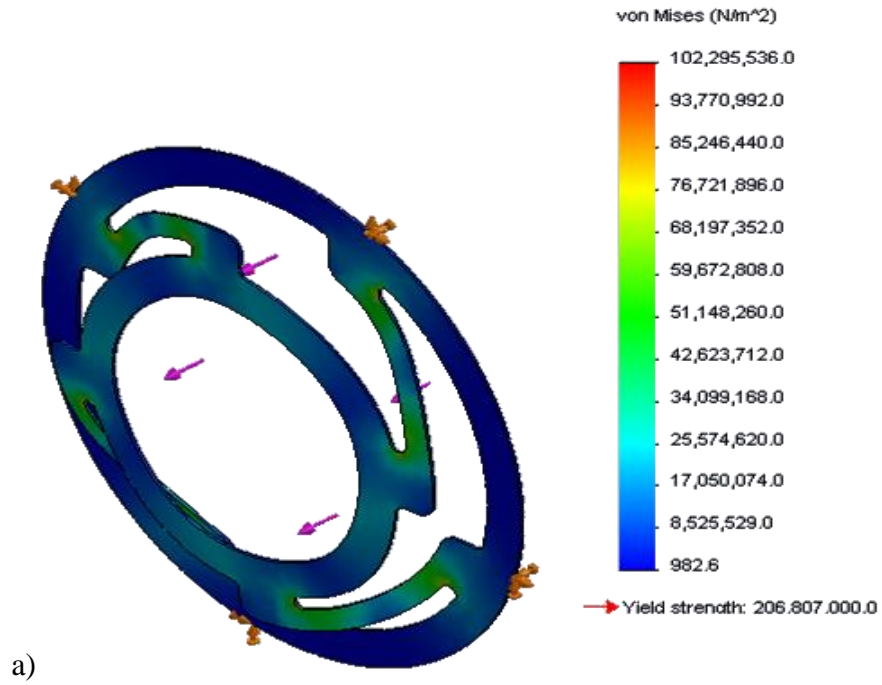


Figure 3.4 (a) Deformation distribution at $\sim 150\mu\text{m}$ displacement and (b) Stress distribution at $150\mu\text{m}$ displacement. Deformation scale for both distributions is 23.67.

The mechanical movement of the voice coil is characterized by measuring the Peak-Peak displacement amplitude of voice coil assembly at different driving currents using a Laser Doppler Vibrometer (LDV).

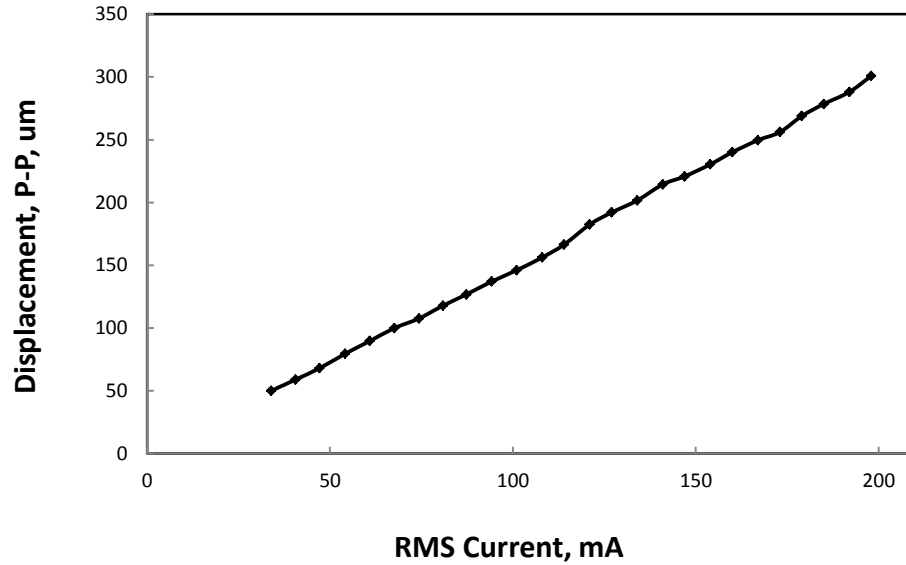


Figure 3.5 Peak-Peak voice coil displacement at different driving current

The movement of the voice coil lens actuator has a linearly proportional relationship with the driving current of the coil (Figure 3.5). A travel distance of $300\mu\text{m}$ is achieved when the coil is driven at sinusoidal current with 200mA Peak-Peak magnitude. Larger travel distance is still possible with a greater driving current.

The tilting of flexure is verified by measuring the displacement at four different corners. The differences of displacement between each corner was less than $5\mu\text{m}$.

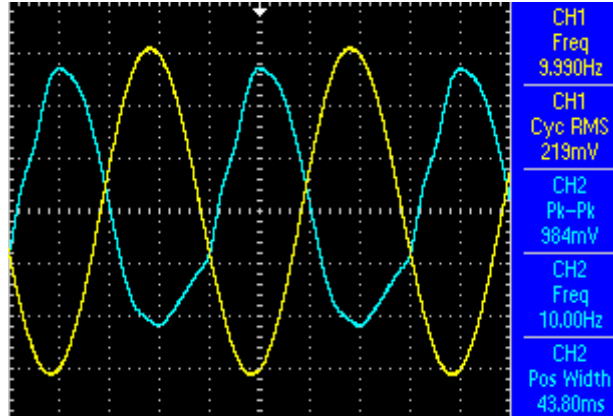


Figure 3.6 Voice coil flexure displacement with driving signal

There is possibly slight non-linearity involved in the movement of the flexure. Figure 3.6 shows the flexure movement under sinusoidal driving current. Channel 1(CH1) in yellow is the driving current signal, and channel 2(CH2) is the flexure movement signal measured by a Laser Doppler Vibrometer. The rising edge of the flexure movement shows slight slope change, which is a sign of non-linearity. The non-linearity may be resolved by increasing the thickness of the flexure.

3.2 Imaging Results

For both vertical and horizontal scanning, because the actuators moves back and forth in each cycle, there are four symmetrically identical images generated within one frame. While the fast axis is operating at 3920Hz and the slow axis at 10Hz, each frame has 392×392 pixels. Only one quarter of each frame is displayed in the software with 196×196 pixels since the remaining images of each frame are symmetrically identical. The scanning frame rate is determined by the slow axis scanning speed since each frame is completed after every slow axis cycle. The developed scanning system typically operates at speed of 10 fps . However, the slow axis scanning speed in both Y and Z directions can be slowed to 8 fps in order to maximize the number of pixels in the image. The minimum scanning speed is currently limited by the

sampling rate of the DAQ card of 2000000 samples/sec. Different scanning speeds would result in variations in image pixels since the fast scanning speed of 3920Hz is fixed. The image pixel in the X scanning direction for the developed system can be calculated using the following equation:

$$Pixels = \frac{f_{fast}}{f_{slow}}$$

where f_{fast} is the fixed X scanning speed of 3920Hz, f_{slow} is the slow scanning speed in the Y or Z directions. The slow scanning speed can only be adjusted to result in an integer number of pixels. There is no maximum frame rate because as the slow axis scanning speed increases, the number of pixels will decrease. However, the frame rate is recommended to be adjusted beyond 20 fps as the pixel number would then be relatively low.

3.2.1 Vertical X-Z Imaging

Vertical X-Z axis scanning is performed with resonant GS and voice coil at 3920Hz and 10 Hz, respectively. Scanning is first conducted on SU-8 photoresist line patterns deposited on a silicon wafer measuring 50 μ m wide and 100 μ m high. Figure 3.7 a) shows the optical profile image of the SU-8 deposit using a Wyko optical profiler (Veeco Instrument Inc.) and Figure 3.7 b) shows the vertical scanning image of the SU-8 cross-section. Because only the upper surface of the SU-8 deposit and the silicon wafer surface are reflective, there is only light reflection on these surfaces. The upper line pattern in Figure 3.7 b) is the SU-8 surface, and the lower line pattern is the silicon wafer surface.

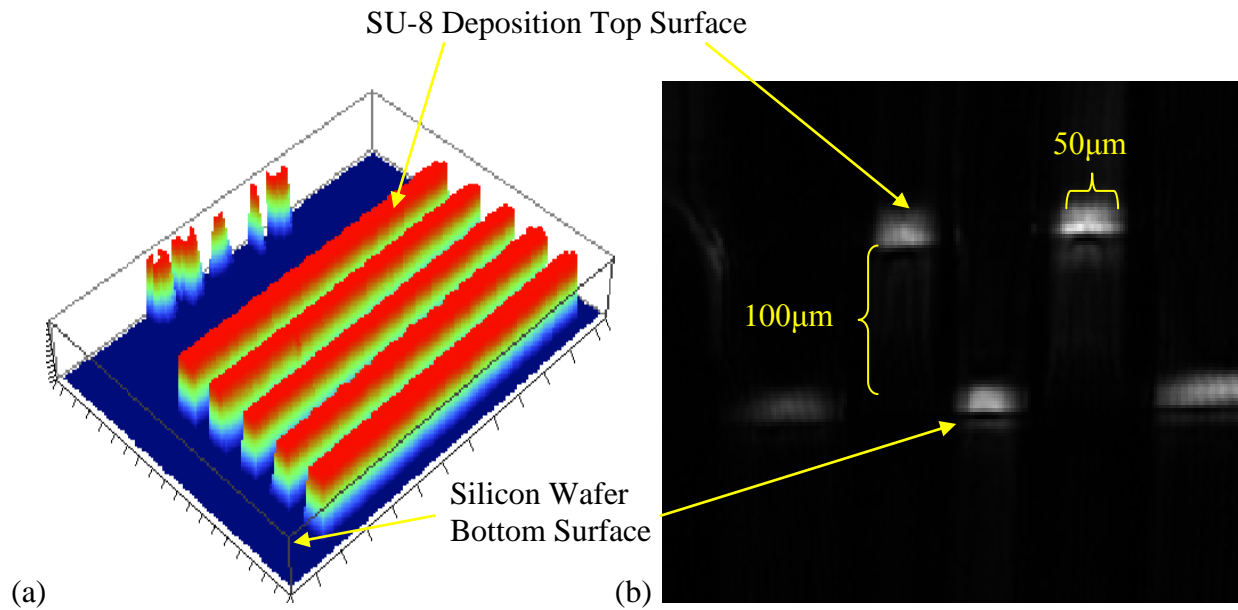


Figure 3.7 (a) Optical profile image of 50 μm wide, 100 μm high, SU-8 deposit on a silicon wafer (b) Vertical cross-sectional 2-D scanning of the same SU-8 deposit, scale bar is 50 μm

Cross-sectional scanning is also performed on a biological sample of onion epidermis. The onion epidermis layer is prepared by peeling off the inner surface of the onion and placing it on a microscope slide for imaging. Figure 3.8 a) shows the vertical confocal imaging of the onion epidermis cell using an existing desktop reflectance confocal microscopy system with piezo actuator in Z axis scanning, developed at the BC Cancer Agency [28]. Figure 3.8 b), c) shows the vertical confocal imaging of the onion epidermis cell using our developed system with electromagnetic actuator, and Figure 3.8 d) shows the histology image of the onion sample. The images from the developed hand-held scanner provide similar cellular structures as the existing system, including cellular walls, upper and lower cell boundaries.

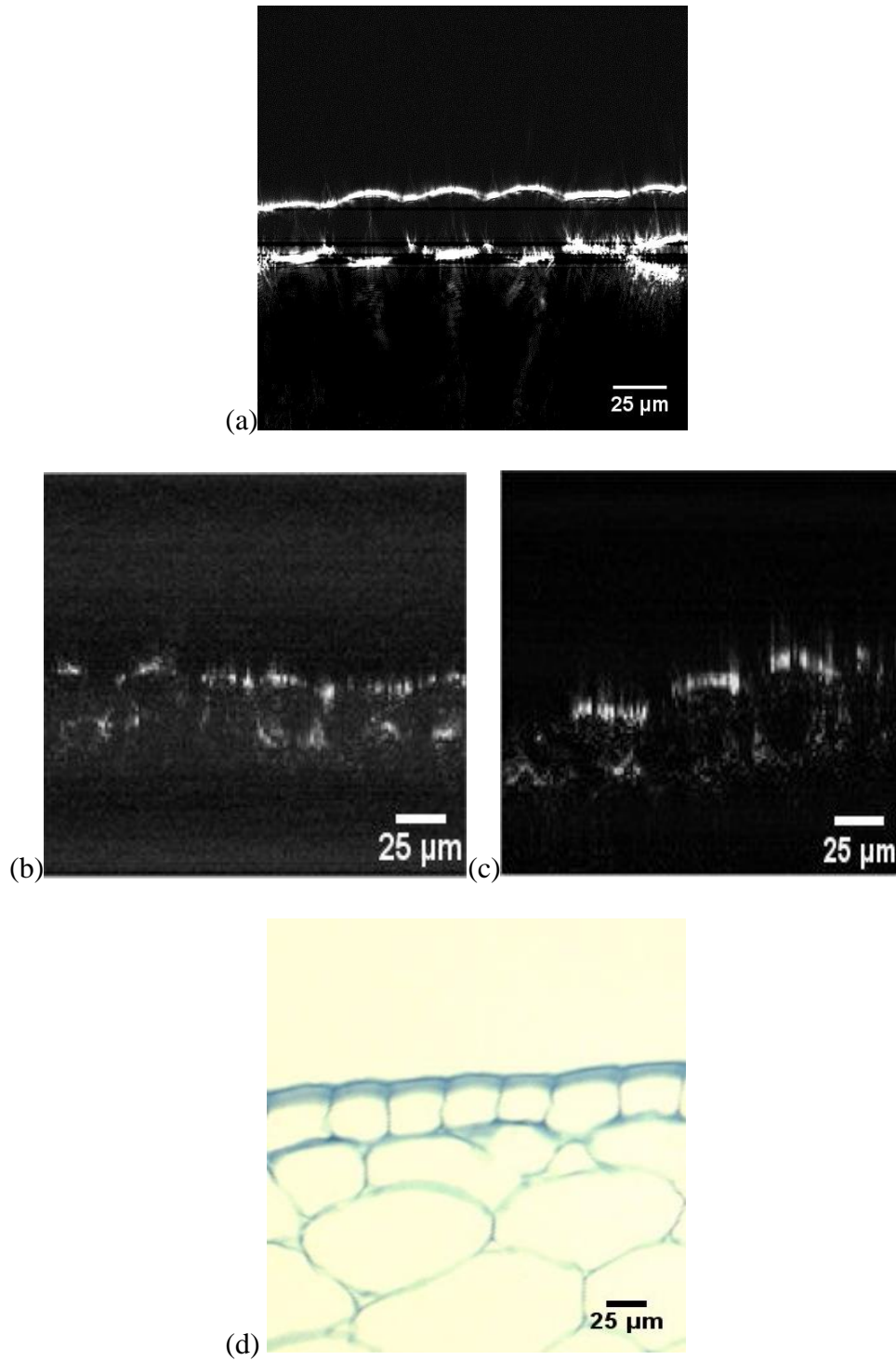


Figure 3.8 (a) Vertical scan of onion epidermis with standard RCM system [28] (b) (c) Vertical scan of onion epidermis with the developed hand-held size system (d) Histology image of onion epidermis, onion sample prepared with Alcian Blue Stain. Image taken using digital microscope

Comparing the onion imaging results with the previous vertical optical sectioning microscanner developed in our lab[12], shown in Figure 3.9, the current developed system shows an improved image quality and more similar cellular structure to the histological image. The previous system's images appear to show irregular cellular line patterns, while the current developed system shows more natural cellular structures.

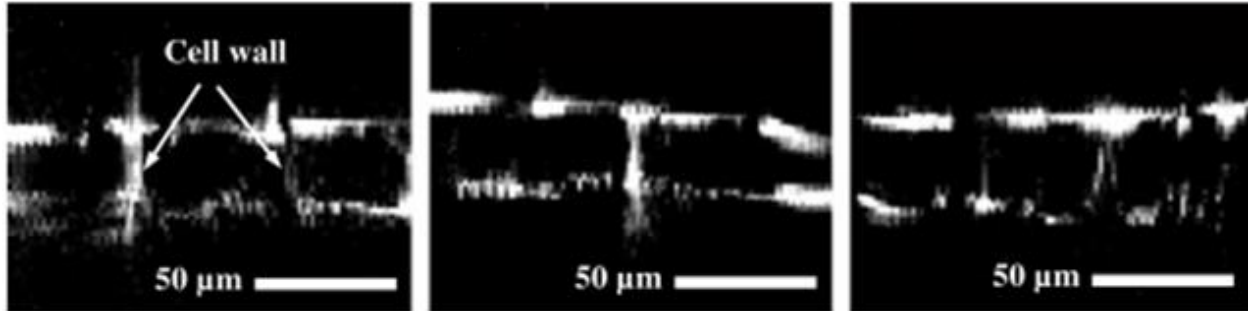


Figure 3.9 Confocal vertical optical section images of onion epidermis from previous developed system[12]

3.2.2 Horizontal X-Y Imaging

Horizontal scanning is performed by actuating the resonant GS and the regular GS together. The imaging is first conducted on a standard USAF 1591 resolution target and 10 μ m grid (Thorlabs R1L1S1P). Figure 3.10 a) shows the image of elements in the USAF resolution target sample group 7. The smallest element feature is the bottom feature, at 227 line pairs per mm. Each line in this element is 2.02 μ m wide. Figure 3.10 b) shows the grid with 10 μ m between every 1.5 μ m wide line. By imaging the standard resolution target, we verified the performance of the developed scanning system with a known subject, and provided reference information in operating the scanner, such as the relationship between scanner control signal amplitude and actual scanning image range.

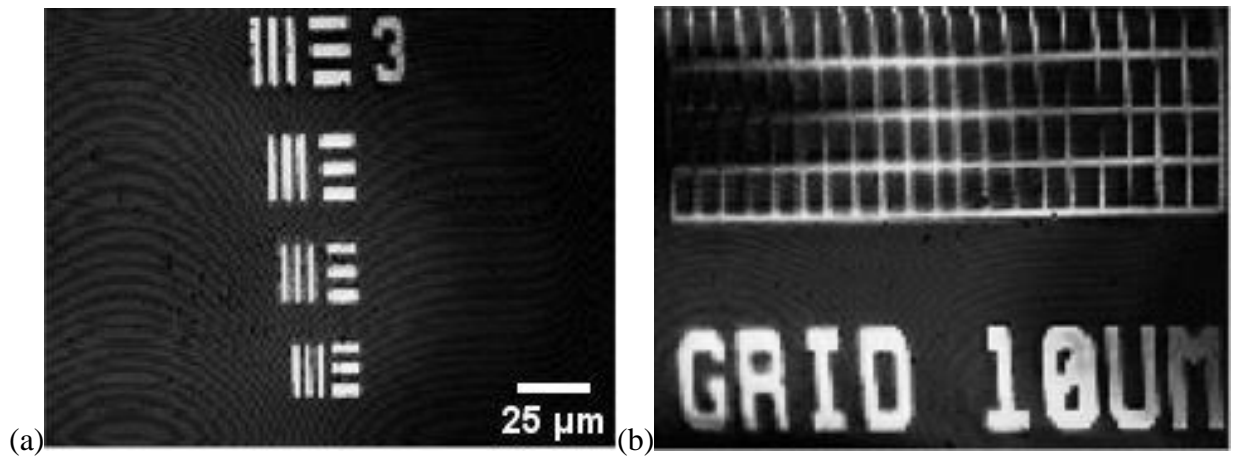
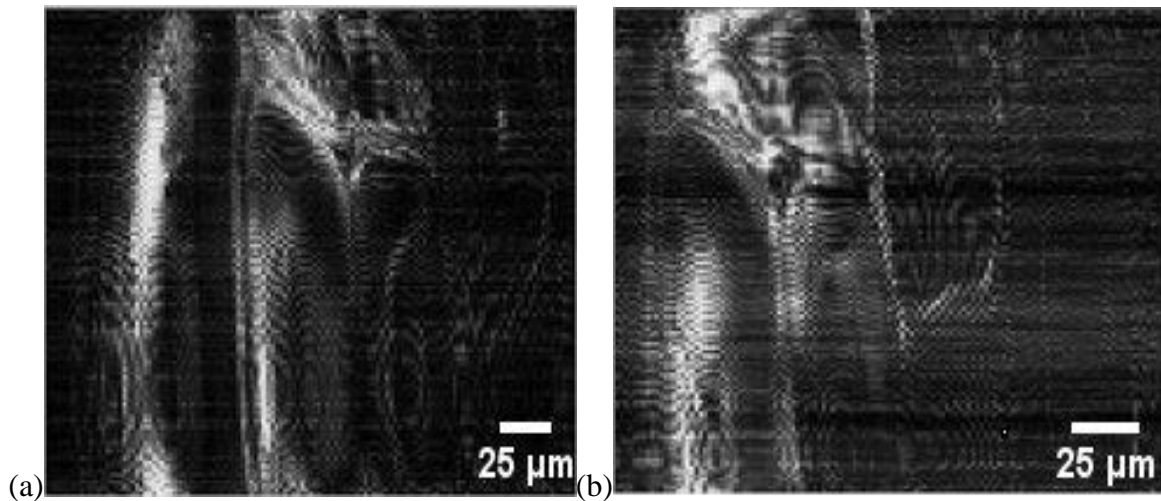


Figure 3.10 (a) Horizontal scan of USAP 1951 resolution target group 7 element 3-6 (b) 10 μm grid with 1.5 μm wide line

Horizontal scan was also performed on onion epidermis. Figure 3.11 a) and b) show the horizontal images scanned by the developed hand-held device and Figure 3.11 c) shows the actual onion epidermis as seen under probe station microscope. Cellular structures including cellular walls are identifiable in the scanned images.



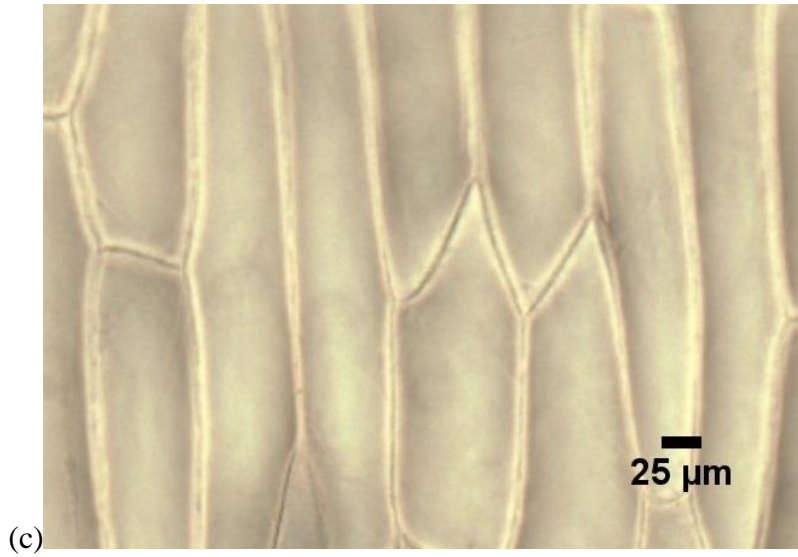


Figure 3.11 (a) and (b) Horizontal scan of onion epidermis using hand-held scanner c) Onion epidermis under microscope

Mouse skin epidermis was imaged with horizontal scanning, as well. The mouse skin was extracted and prepared on a microscope slide. Mouse skin extraction was performed by technician in BC Cancer Agency. Figure 3.12 a) was taken using the standard RCM system [28] on the excised mouse skin and Figure 3.12 b) and c) show the same mouse skin horizontally scanned using the developed hand-held scanner. Similar cellular structure is observed when comparing the image from the standard RCM system with the image from the developed hand-held scanner. The image taken by the standard RCM system appears to be brighter. This may be caused by the larger pinhole size used in the standard RCM system. The pinhole size of the developed hand-held scanner is 4μm while the pinhole used in the standard RCM system is around 20μm. Larger pinhole would allow more reflected light to pass through, hence increasing the light intensity to be detected.

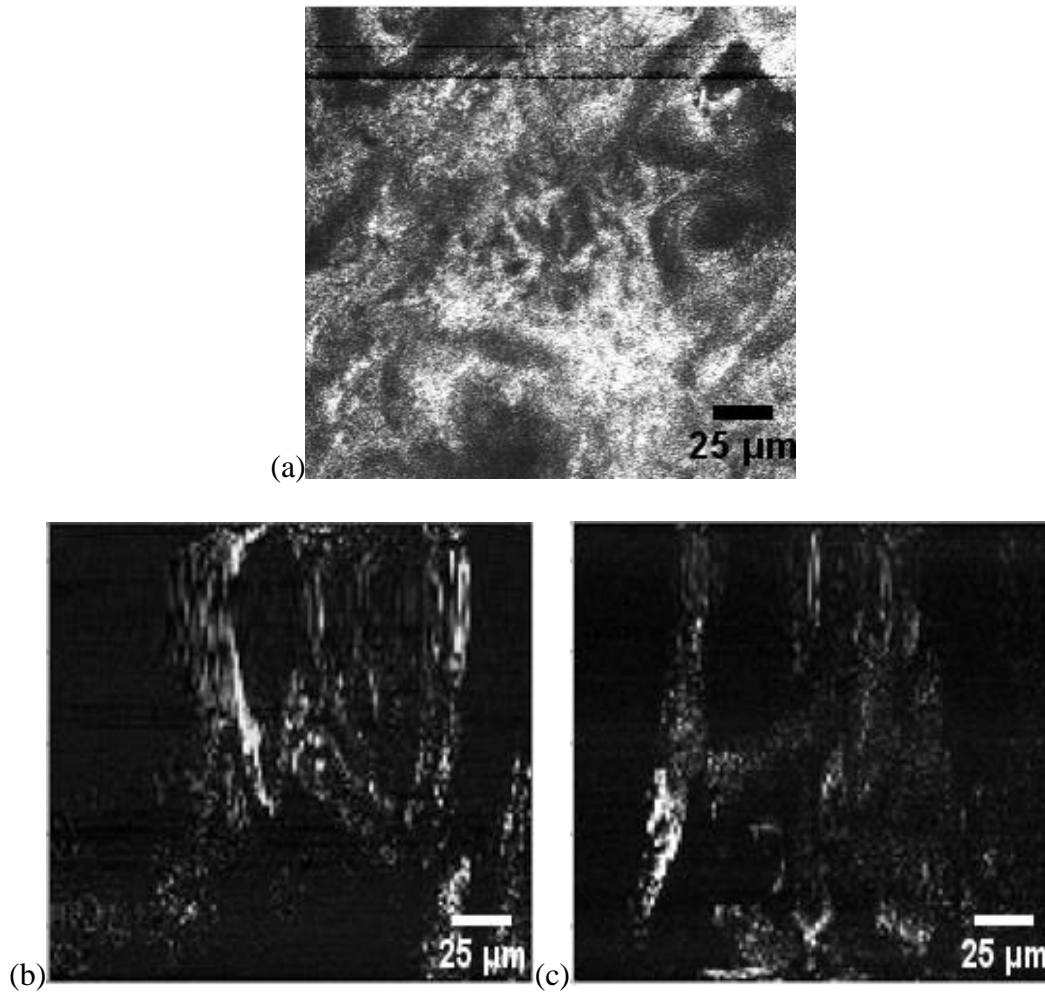


Figure 3.12 (a) Mouse skin epidermis horizontal confocal image with standard RCM system [28] (b) and (c)

Hand-held horizontal scanning confocal image of mouse skin epidermis

Chapter 4: Conclusion and Future Work

4.1 Summary

In chapter 1, we reviewed background on skin cancer, and current methods for skin cancer detection. Different non-invasive optical methods for imaging were compared and the advantages of reflectance microscopy for skin imaging were demonstrated. The research objective and thesis structure were also reviewed.

In chapter 2, we demonstrated the vertical and horizontal scanning principles, as well as the actuators used for scanning. The design and assembly of the novel voice coil actuator for objective lens was discussed. In addition, the design and layout of the entire scanning system, including the desktop portion and hand-held portion were presented. The methods used for image processing and software control were also discussed.

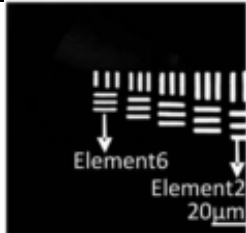
In chapter 3, the scanning system characteristics were first demonstrated, including axial and lateral resolutions. The voice coil performance was illustrated, as well. Imaging results in horizontal and vertical directions were also shown. Imaging was first performed with standard targets, and then with biological tissues, namely onion epidermis and mouse skin. The observed images were compared with tissue structures taken with standard microscopes and the existing confocal scanning system.

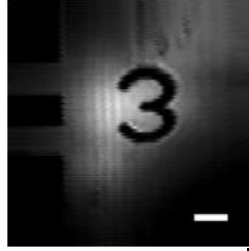
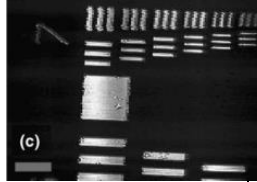
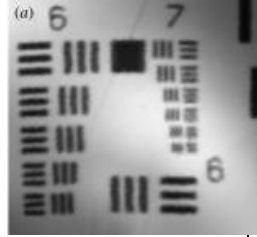

In conclusion, we successfully developed a hand-held size real time confocal optical scanner for both cross-sectional and horizontal scanning at $1\mu\text{m}\times 8\mu\text{m}$ scanning resolutions with 136×136

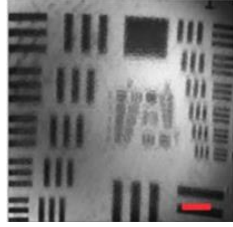
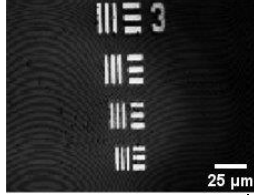
pixels at 10 frames per second. A novel voice coil actuator was designed and used to actuate the objective lens for depth scanning. Biological tissue imaging in both horizontal and vertical directions was verified with mouse skin and onion epidermis. The developed hand-held system provides the potential to perform both horizontal and vertical near real time optical sectioning in a portable setting. The real time scanning speed allows the user to observe the skin image without delay, and therefore, enhance the efficiency and usability of the developed hand-held system. The resolution allows the scanned image to show cellular structures. With further improvements on the optics, the scanner will be capable of showing sub-cellular structures.

The Table 4.1 compares different design and performances of several other reflectance confocal microscopy systems with our developed hand-held system.

Table 4.1 Performance comparison of reflectance confocal microscopy systems.

| Actuation mechanism, scanning dimensions | Resolution | Scanning speed | USAF Target sample image | Portable ? | Reference |
|---|--|------------------|--|---------------|-----------|
| MEMS mirror (X,Y) and MEMS lens actuator(Z), 3D | Axial: 9.0 μm Lateral: 1.2 μm | Frame rate: 1fps |  <p>Scale bar: 20 μm</p> | No | [23] |

| Actuation mechanism, scanning dimensions | Resolution | Scanning speed | USAF Target sample image | Portable ? | Reference |
|--|---|------------------------|--|---------------|-----------|
| MEMS mirror(X,Y), 2D | Axial: 6.68 μm Lateral: 3.94 μm | Frame rate: 8 fps |  <p>Scale bar: 50 μm</p> | No | [17] |
| MEMS mirror(X,Y), 2D | Axial: 4.2 μm Lateral: 0.5 μm | Frame rate: 3-5 fps |  <p>Scale bar: 25 μm</p> | Yes | [15] |
| MEMS mirror(X,Y), 2D | Axial: 5.8 μm Lateral: 3 μm | Frame rate: 2 pfs |  | Yes | [16] |
| Two Galvo mirrors(X,Y) and piezoelectric device(Z), 3D | Axial: N/A Lateral: N/A | Frame rate: 30 fps |  | No | [22] |
| Polygon mirror (X) and galvo mirror(Y), 2D | Axial: 3-5 μm Lateral: 0.5-1 μm | Frame rate: 30 fps | N/A | No | [10] |
| Prismatic scanner(X,Y), 2D | Axial: 1.7 \pm 0.1 μm Lateral: 1.0 \pm 0.1 μm | Frame rate: N/A | N/A | No | [32] |

| Actuation mechanism, scanning dimensions | Resolution | Scanning speed | USAF Target sample image | Portable ? | Reference |
|--|---|-----------------------------|---|---------------|---------------|
| MEMS mirror(X,Y), | Axial: N/A Lateral: N/A | Frame rate: 1.3 fps |  Scale bar: 2mm | No | [33] |
| Two galvo mirrors(X,Y) and electromagnetic actuator(Z), 3D | Axial: 5-8 μm Lateral: 0.9 - 1.1 μm | Frame rate: 8-20 fps |  Scale bar: 25 μm | Yes | Our system |

Our developed system provides high resolution and fast scanning speeds, along with portability, for quality images.

4.2 Future Work

The optical performance of the developed device can be further improved with custom made objective lens optics. Larger NA of the objective lens is desired to increase the resolution in lateral and axial directions. In order to achieve larger NA, it will require to either increase the clear aperture of the objective lens, or decrease the focal distance. However, this will cause an increase in the overall device size and a decrease in the available working distance between the objective lens to the sample. There has been some preliminary work done in making a custom objective lens with higher resolution. Our research group is currently collaborating with the College of Optical Science at the University of Arizona to design a suitable focal lens with

higher optical performance. With improved resolution, in vivo human skin imaging is also desired to further assess the imaging quality of the developed system. The mechanical interface between the hand-held device and the human skin will require a stable and accurate mounting method. Ultrasound gel or other contacting liquid, such as water, can also be used as imaging medium to better match the refractive index at the skin surface.

There is slight interference pattern and background noise appearing in the current developed system image. The image quality may be improved with better optical alignment and improved light filtering. More linear movement of the voice coil, with reduced non-linearity, may also enhance the image quality.

It is also possible to use a smaller regular GS and a smaller mirror for Y-axis scanning in the hand-held portion of the device, to further reduce the overall size. The regular GS used in the current setup has a 15mm clear aperture mirror. Since the resonant GS has clear aperture of 12mm and the effective beam diameter is 8.7mm when placed at 45° , the regular GS aperture size can be reduced to 12mm as well. The use of a smaller mirror and smaller regular GS will cause further size reduction of the hand-held device because the mounting for the regular GS can be smaller as well.

Furthermore, the horizontal and vertical imaging capabilities provide the opportunity to perform real time 3-D imaging. The control and imaging software can be modified to synchronize the driving signals, process and construct a 3-D image volume from a stack of 2D images, either from the horizontal plane or the vertical plane. If the 3-D image volume is constructed from

horizontal sectioning, a series of horizontal images can be recorded by actuating the voice coil even slower than the regular GS frequency. If the 3-D image volume is constructed from vertical sectioning, a series of vertical images can be recorded by actuating the regular GS slower than the voice coil.

Bibliography

- [1] Rogers H. W., Weinstock M. a, Harris A. R., Hinckley M. R., Feldman S. R., Fleischer A. B., and Coldiron B. M., 2010, "Incidence estimate of nonmelanoma skin cancer in the United States, 2006.," *Archives of dermatology*, 146(3), pp. 283–7.
- [2] Chen S. C., Bravata D. M., Weil E., and Olkin I., 2001, "A comparison of dermatologists' and primary care physicians' accuracy in diagnosing melanoma: a systematic review.," *Archives of dermatology*, 137(12), pp. 1627–34.
- [3] Zuber T. J., 2002, "Punch biopsy of the skin.," *American family physician*, 65(6), pp. 1155–8, 1161–2, 1164.
- [4] Nischal K. C., and Khopkar U., 2005, "Dermoscope," *Indian J Dermatol Venereol Leprol*, 71(4), pp. 300–303.
- [5] Zysk A. M., Nguyen F. T., Oldenburg A. L., Marks D. L., and Boppart S. a, 2013, "Optical coherence tomography: a review of clinical development from bench to bedside.," *Journal of biomedical optics*, 12(5), p. 051403.
- [6] Nehal K. S., Gareau D., and Rajadhyaksha M., 2008, "Skin imaging with reflectance confocal microscopy.," *Seminars in cutaneous medicine and surgery*, 27(1), pp. 37–43.
- [7] Thiberville L., Moreno-Swirc S., Vercauteren T., Peltier E., Cav éC., and Bourg Heckly G., 2007, "In vivo imaging of the bronchial wall microstructure using fibered confocal fluorescence microscopy.," *American journal of respiratory and critical care medicine*, 175(1), pp. 22–31.

- [8] Konig K., and Riemann I., 2003, “High-resolution multiphoton tomography of human skin with subcellular spatial resolution and picosecond time resolution.,” *Journal of biomedical optics*, 8(3), pp. 432–9.
- [9] “Confocal Microscopy”, Internet: https://www.jic.ac.uk/microscopy/more/T5_8.htm, [Nov. 24th, 2014]
- [10] M. Rajadhyaksha, R. R. Anderson, and R. H. Webb, “Video-rate confocal scanning laser microscope for imaging human tissues in vivo.,” *Appl. Opt.*, vol. 38, no. 10, pp. 2105–15, Apr. 1999.
- [11] K. S. Nehal, D. Gareau, and M. Rajadhyaksha, “Skin imaging with reflectance confocal microscopy.,” *Semin. Cutan. Med. Surg.*, vol. 27, no. 1, pp. 37–43, Mar. 2008.
- [12] H. Mansoor, H. Zeng, K. Chen, Y. Yu, J. Zhao, and M. Chiao, “Vertical optical sectioning using a magnetically driven confocal microscanner aimed for in vivo clinical imaging.,” *Opt. Express*, vol. 19, no. 25, pp. 25161–72, Dec. 2011.
- [13] H. Search, C. Journals, A. Contact, M. Iopscience, and I. P. Address, “Confocal optical microscopy,” vol. 427.
- [14] C. a Patil, C. L. Arrasmith, M. a Mackanos, D. L. Dickensheets, and A. Mahadevan-Jansen, “A handheld laser scanning confocal reflectance imaging-confocal Raman microspectroscopy system.,” *Biomed. Opt. Express*, vol. 3, no. 3, pp. 488–502, Mar. 2012.
- [15] K. Kumar, R. Avritscher, Y. Wang, N. Lane, D. C. Madoff, T.-K. Yu, J. W. Uhr, and X. Zhang, “Handheld histology-equivalent sectioning laser-scanning confocal optical

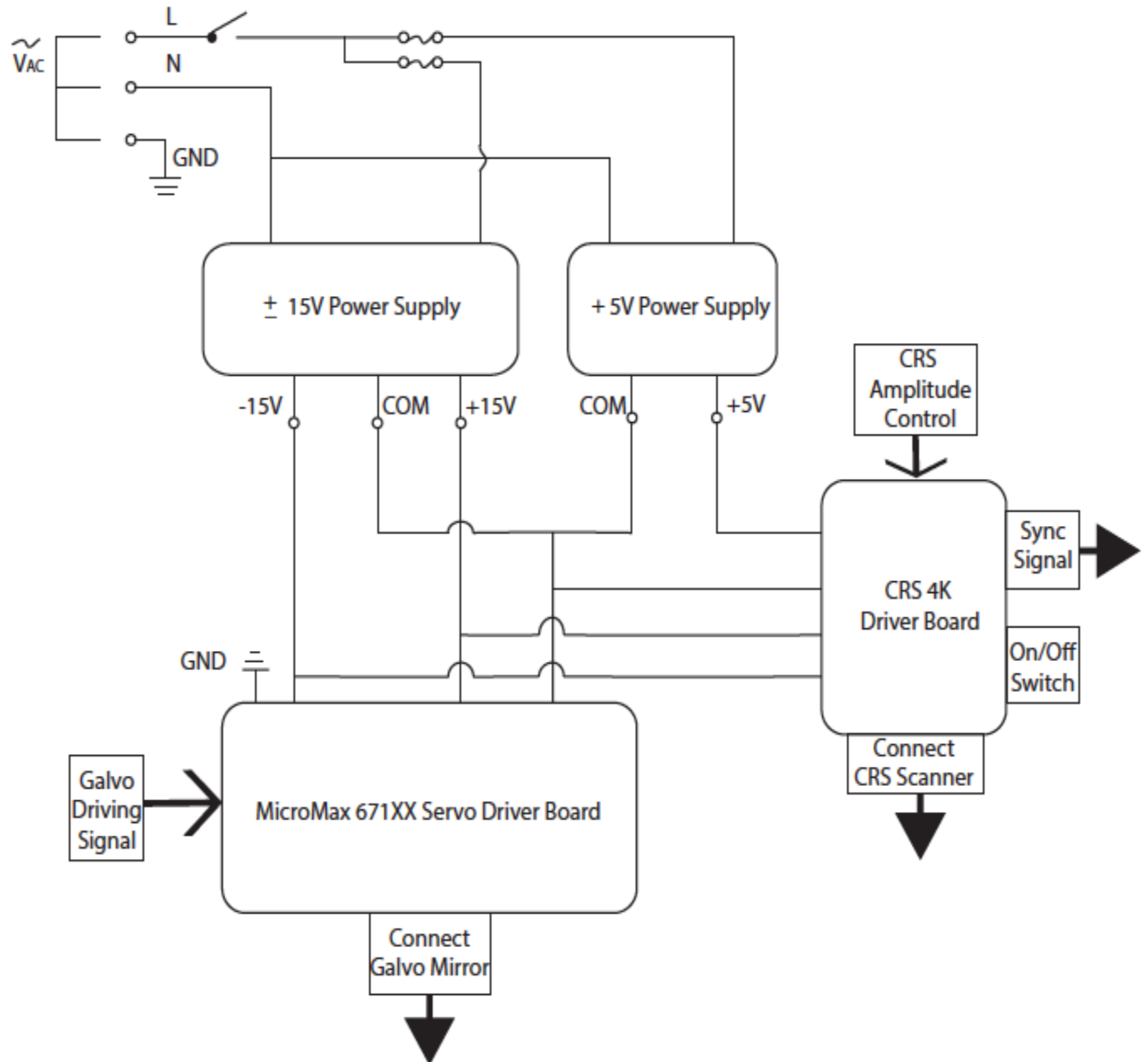
- microscope for interventional imaging,” *Biomed. Microdevices*, vol. 12, no. 2, pp. 223–33, Apr. 2010.
- [16] Y. Wang, M. Raj, H. S. McGuff, G. Bhawe, B. Yang, T. Shen, and X. Zhang, “Portable oral cancer detection using a miniature confocal imaging probe with a large field of view,” *J. Micromechanics Microengineering*, vol. 22, no. 6, p. 065001, Jun. 2012.
- [17] H. Ra, W. Piyawattanametha, Y. Taguchi, D. Lee, M. J. Mandella, and O. Solgaard, “Two-Dimensional MEMS Scanner for Dual-Axes Confocal Microscopy,” *J. Microelectromechanical Syst.*, vol. 16, no. 4, pp. 969–976, 2007.
- [18] H. Mansoor, H. Zeng, I. T. Tai, J. Zhao, and M. Chiao, “A handheld electromagnetically actuated fiber optic raster scanner for reflectance confocal imaging of biological tissues,” *IEEE Trans. Biomed. Eng.*, vol. 60, no. 5, pp. 1431–8, May 2013.
- [19] M. J. Booth, R. Juskaitytis, and T. Wilson, “Spectral confocal reflection microscopy using a white light source,” *J. Eur. Opt. Soc. Rapid Publ.*, vol. 3, p. 08026, Aug. 2008.
- [20] T. D. Wang, C. H. Contag, M. J. Mandella, N. Y. Chan, and G. S. Kino, “Dual-axes confocal microscopy with post-objective scanning and low-coherence heterodyne detection,” *Opt. Lett.*, vol. 28, no. 20, pp. 1915–7, Oct. 2003.
- [21] Z. Qiu, Z. Liu, X. Duan, S. Khondee, B. Joshi, M. J. Mandella, K. Oldham, K. Kurabayashi, and T. D. Wang, “Targeted vertical cross-sectional imaging with handheld near-infrared dual axes confocal fluorescence endomicroscope,” *Biomed. Opt. Express*, vol. 4, no. 2, pp. 322–30, Feb. 2013.

- [22] N. Callamaras and I. Parker, "Construction of a confocal microscope for real-time x-y and x-z imaging.," *Cell Calcium*, vol. 26, no. 6, pp. 271–9, Dec. 1999.
- [23] L. Liu and H. Xie, "3-D Confocal Laser Scanning Microscopy Based on a Full-MEMS Scanning System," *IEEE Photonics Technol. Lett.*, vol. 25, no. 15, pp. 1478–1480, Aug. 2013.
- [24] M. J. Sanderson, "Acquisition of Multiple Real-Time Images for Laser Scanning Microscopy MIRRORS," vol. 18, no. 4, pp. 2–6, 2004.
- [25] Y. Chen, C. Fuh, and P. Tung, "Application of voice coil motors in active dynamic vibration absorbers," *IEEE Trans. Magn.*, vol. 41, no. 3, pp. 1149–1154, Mar. 2005.
- [26] L. Xu, X. Tian, X. Li, G. Shang, and J. Yao, "Geometric distortion correction for sinusoidally scanned images," *Measurement Science and Technology*, vol. 22, no. 11, p. 114023, Nov. 2011.
- [27] R. W. Cole, T. Jinadasa, and C. M. Brown, "Measuring and interpreting point spread functions to determine confocal microscope resolution and ensure quality control.," *Nat. Protoc.*, vol. 6, no. 12, pp. 1929–41, Dec. 2011.
- [28] H. Wang, A. M.D. Lee, Z. Frehlick, H. Lui, D. I. McLean, S. Tang and H. Zeng, "Perfectly registered multiphoton and reflectance confocal video rate imaging of in vivo human skin," *J. Biophoton.*, vol. 6, no. 4, pp. 305–309, Apr. 2013.
- [29] Y. Yu, "Excitation/Emission spectroscopy with multi-channel imaging guidance for skin disease diagnosis," MS Thesis, Univ. of BC, Vancouver, BC, 2013

- [30] H. Ra, W. Piyawattanametha, M. J. Mandella, P.-L. Hsiung, J. Hardy, T. D. Wang, C. H. Contag, G. S. Kino, and O. Solgaard, "Three-dimensional in vivo imaging by a handheld dual-axes confocal microscope," *Opt. Express*, vol. 16, no. 10, p. 7224, May 2008.
- [31] C. L. Arrasmith, D. L. Dickensheets, and A. Mahadevan-Jansen, "MEMS-based handheld confocal microscope for in-vivo skin imaging.," *Opt. Express*, vol. 18, no. 4, pp. 3805–19, Feb. 2010.
- [32] P. J. Dwyer, C. a DiMarzio, J. M. Zavislan, W. J. Fox, and M. Rajadhyaksha, "Confocal reflectance theta line scanning microscope for imaging human skin in vivo.," *Opt. Lett.*, vol. 31, no. 7, pp. 942–4, Apr. 2006.
- [33] Y. Wang, S. Bish, J. W. Tunnell, and X. Zhang, "MEMS scanner enabled real-time depth sensitive hyperspectral imaging of biological tissue.," *Opt. Express*, vol. 18, no. 23, pp. 24101–24108, 2010.

Appendices

Appendix A Electrical Driver Box Layout for Galvo Mirrors

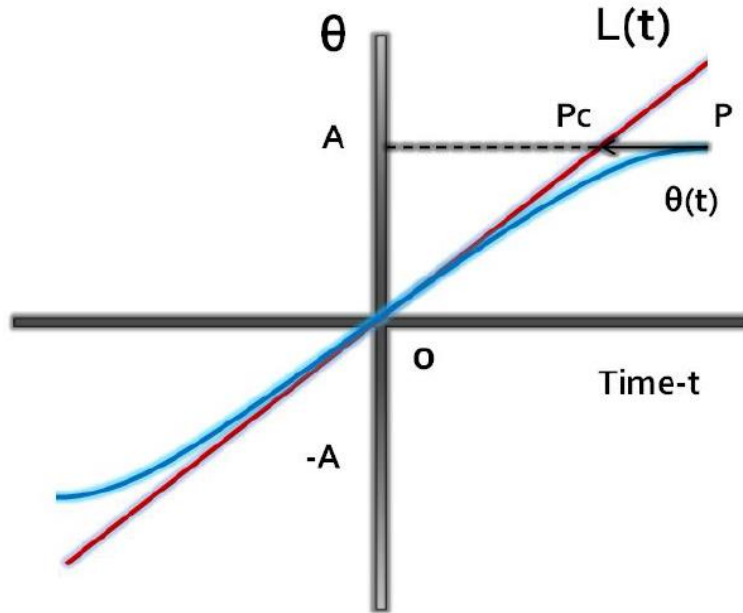


List of Components for Electrical Control Box:

| Item Part Number (Digikey) | Description | Quantity |
|---------------------------------------|-------------------------------------|-----------------|
| 271-2248-ND | PWR SPLY LINEAR SINGLE 5V@1.5A | 1 |
| HCC15-3-AG | LNR SUP DBL OUT 12/15V CASE CC | 1 |
| CCM1698-ND | MODULE POWER ENTRY FLANGE 6A | 1 |
| CKC2011-ND | SWITCH ROCKER SPST QC TERM W/MRK | 3 |
| CKN2068-ND | SWITCH ROCKER ILLUM 10A GRN | 1 |
| F2511-ND | FUSE 250V FAST 3AG 4A CART | 5 |
| 283-2715-ND | FUSE HLDR RT ANGL SLDR/QUK HTB-4 | 5 |

Appendix B Distortion Correction

Image distortion is corrected by linearizing the sinusoidal waveform. As seen in the figure,



the blue curve is the actual sinusoidal scanning pattern and red line is the ideal linear scanning pattern. The linearization process relocates the pixels distributed along the actual pattern to the ideal linear pattern. $\theta(t)$: variable representing the actual scanning angle of X-axis scanner at a certain time point (t); A : a certain value of $\theta(t)$; $L(t)$: variable representing the corrected angle of X-axis scanner for the ideal linear scan [29].

The image distortion correction is embedded in the Labview program as a call library function.

The correction code is saved as a .dll file for Labview program to call.

Source code for image distortion correction:

```
#include "extcode.h"

#include <math.h>

_declspec(dllexport) void correct_image(double pre_img[],double post_img[],

        int array_length_row,

        int array_length_col);

_declspec(dllexport) void correct_image(double pre_img[],double post_img[],

        int array_length_row,

        int array_length_col)

{

    int i, j, i_new,j_new;

    double pi=3.1415926;

    int mid_row;

    int mid_col;

    double ph_row,ph_col,c_row,c_col;

    mid_row = array_length_row / 2;

    mid_col =array_length_col / 2;

    for(i = 0; i < array_length_row; i++)

    {
```

```

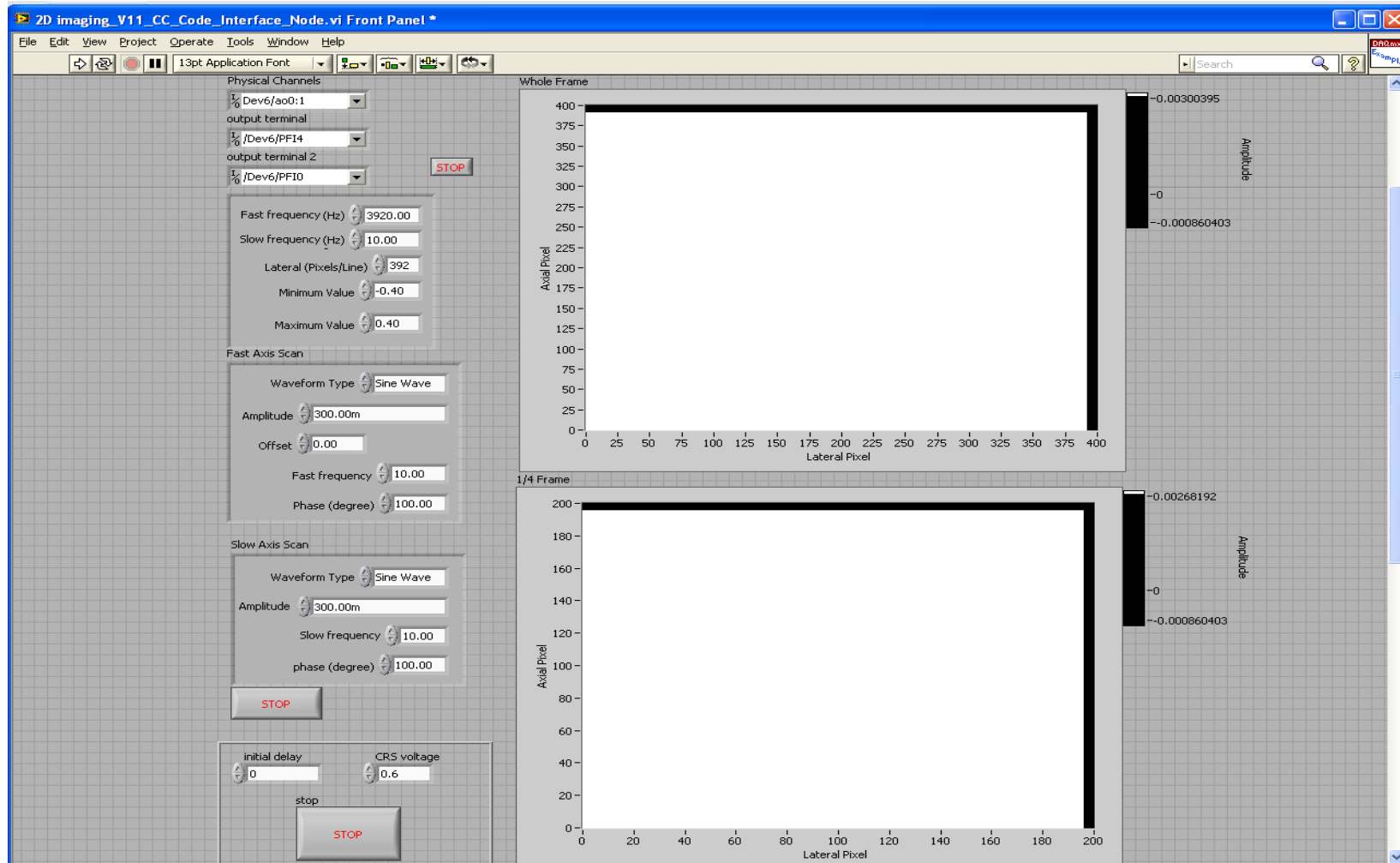
for(j = 0; j < array_length_col; j++)
{
    ph_col=(pi/array_length_col)*(j-mid_col);
    ph_row=(pi/array_length_row)*(i-mid_row);
    c_row=ph_row/sin(ph_row);
    c_col=ph_col/sin(ph_col);

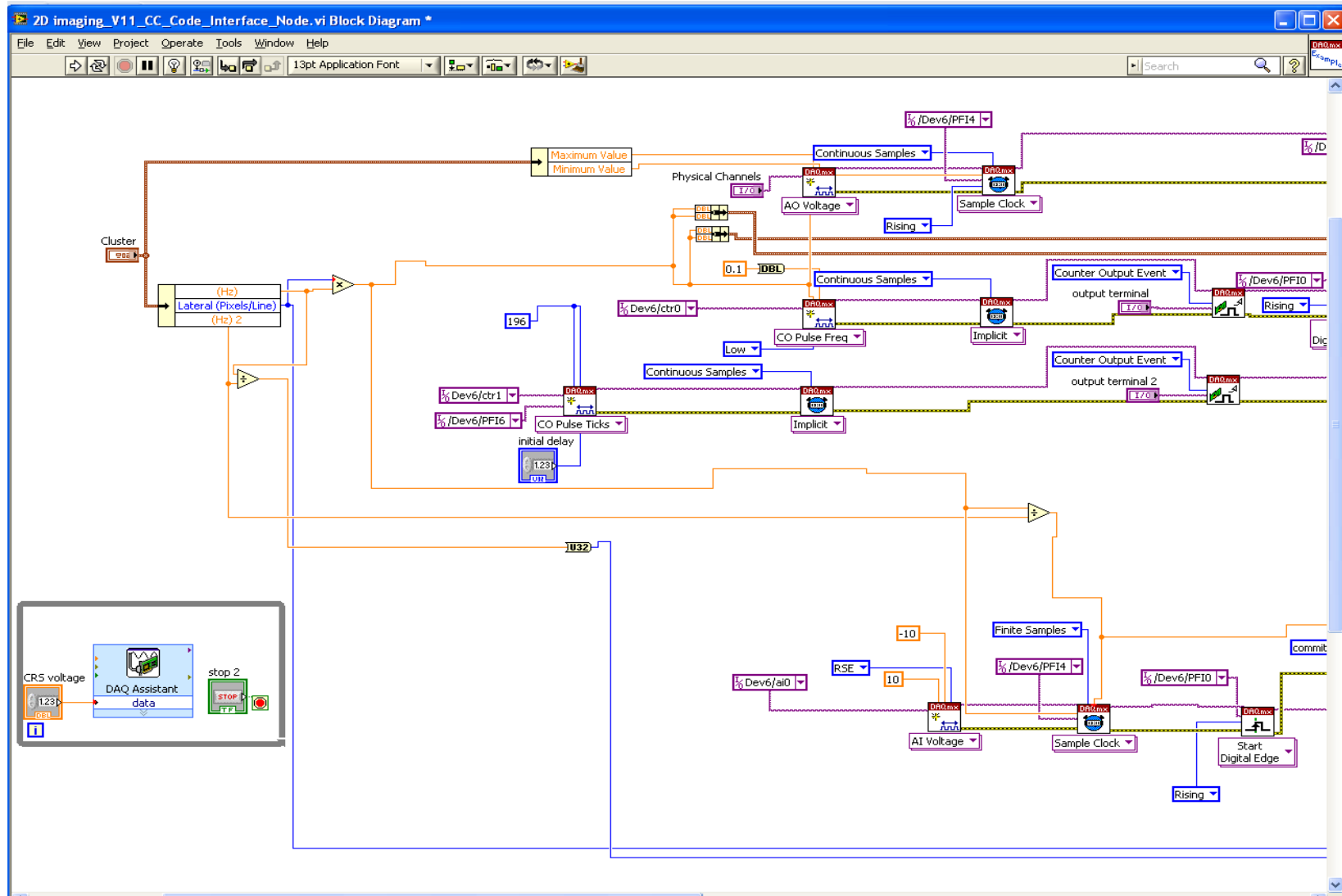
    i_new=mid_row+ (i-mid_row)/c_row;
    j_new=mid_col+ (j-mid_row)/c_col;

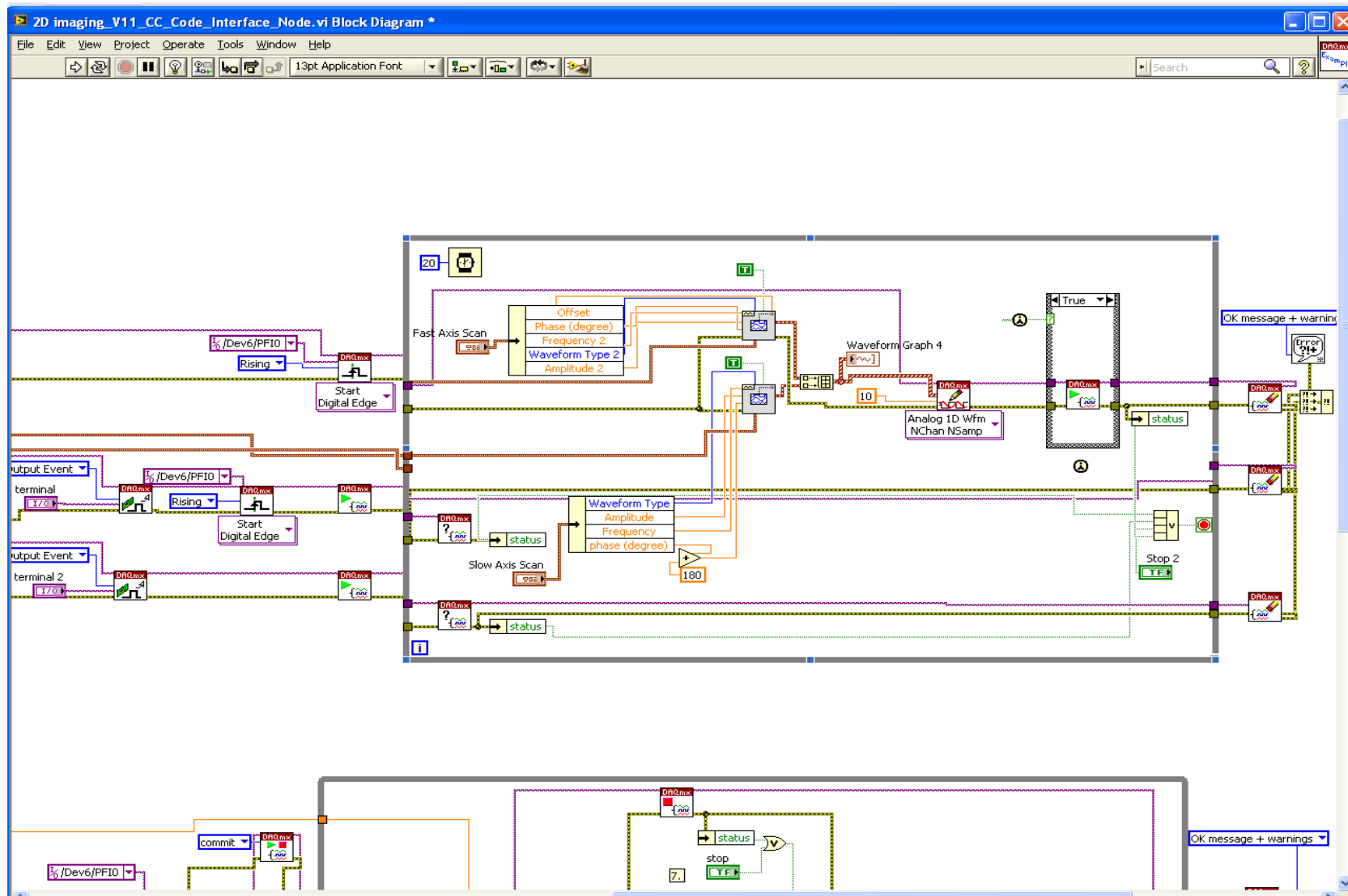
    if(i_new<array_length_row  &&  j_new<array_length_col  &&  i_new>0  &&
j_new>0)
    {
        post_img[(i_new*array_length_col)+j_new]
pre_img[(i*array_length_col)+j];
    }
}
}
}

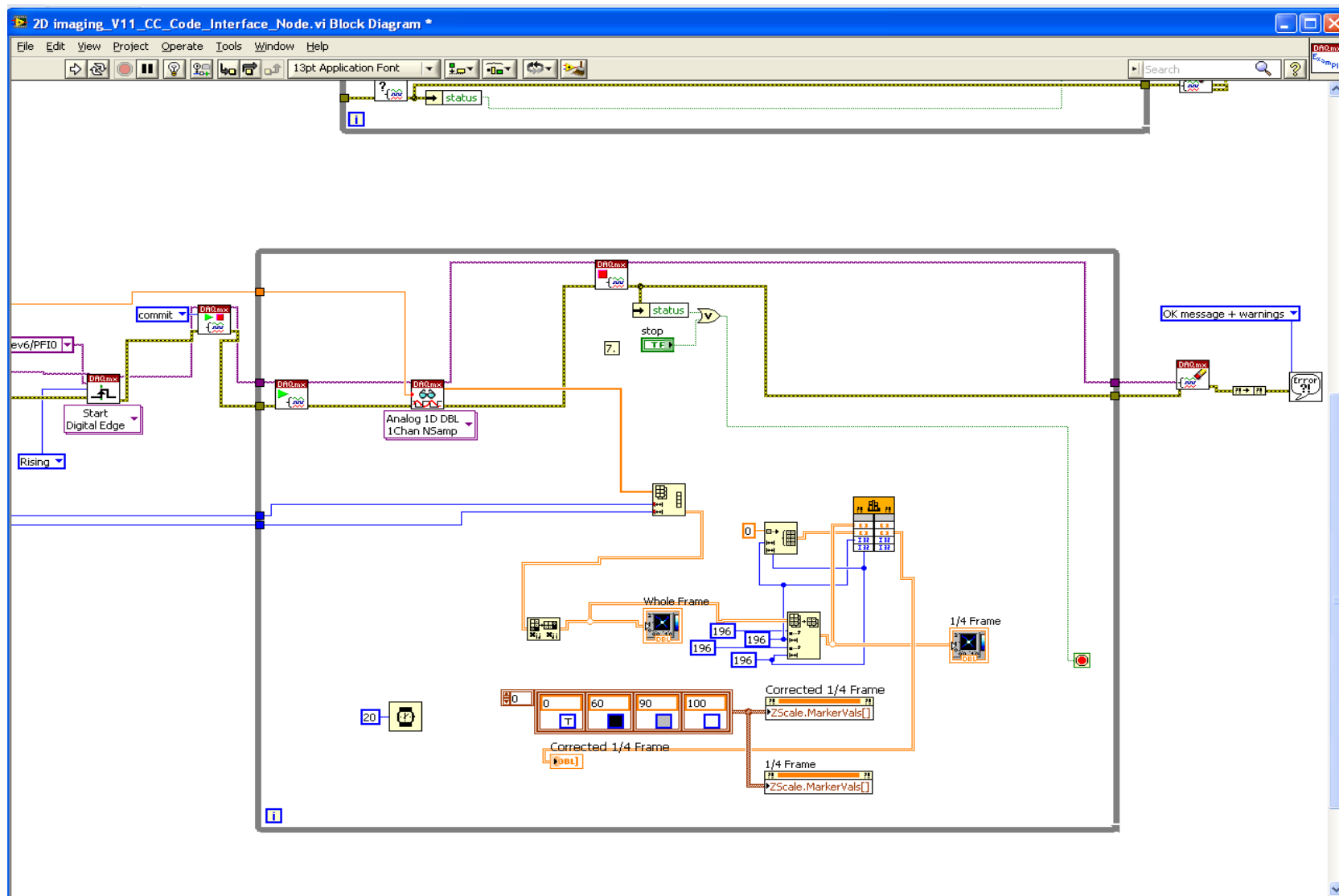
```

Appendix C Imaging and Control Labview Software

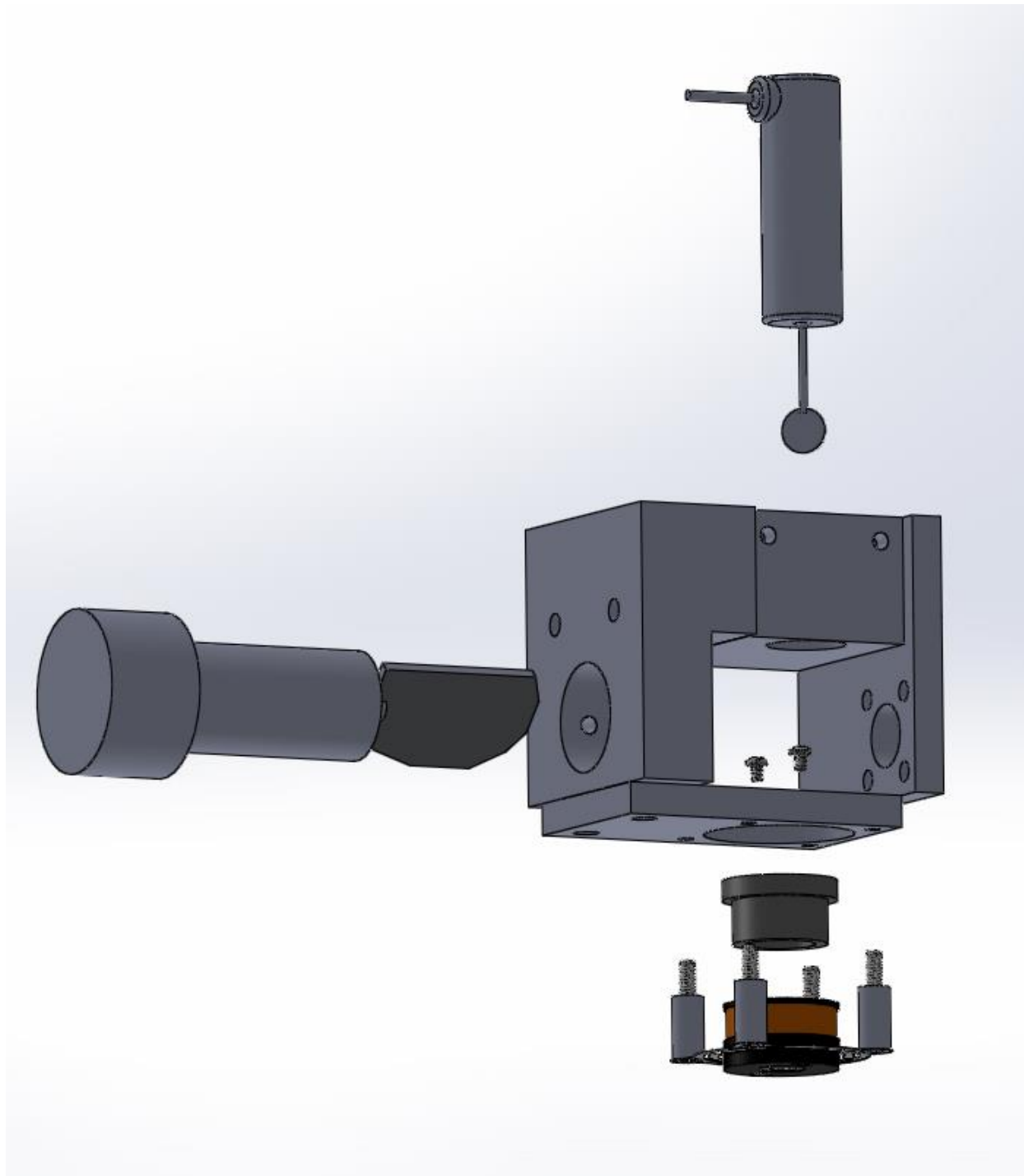


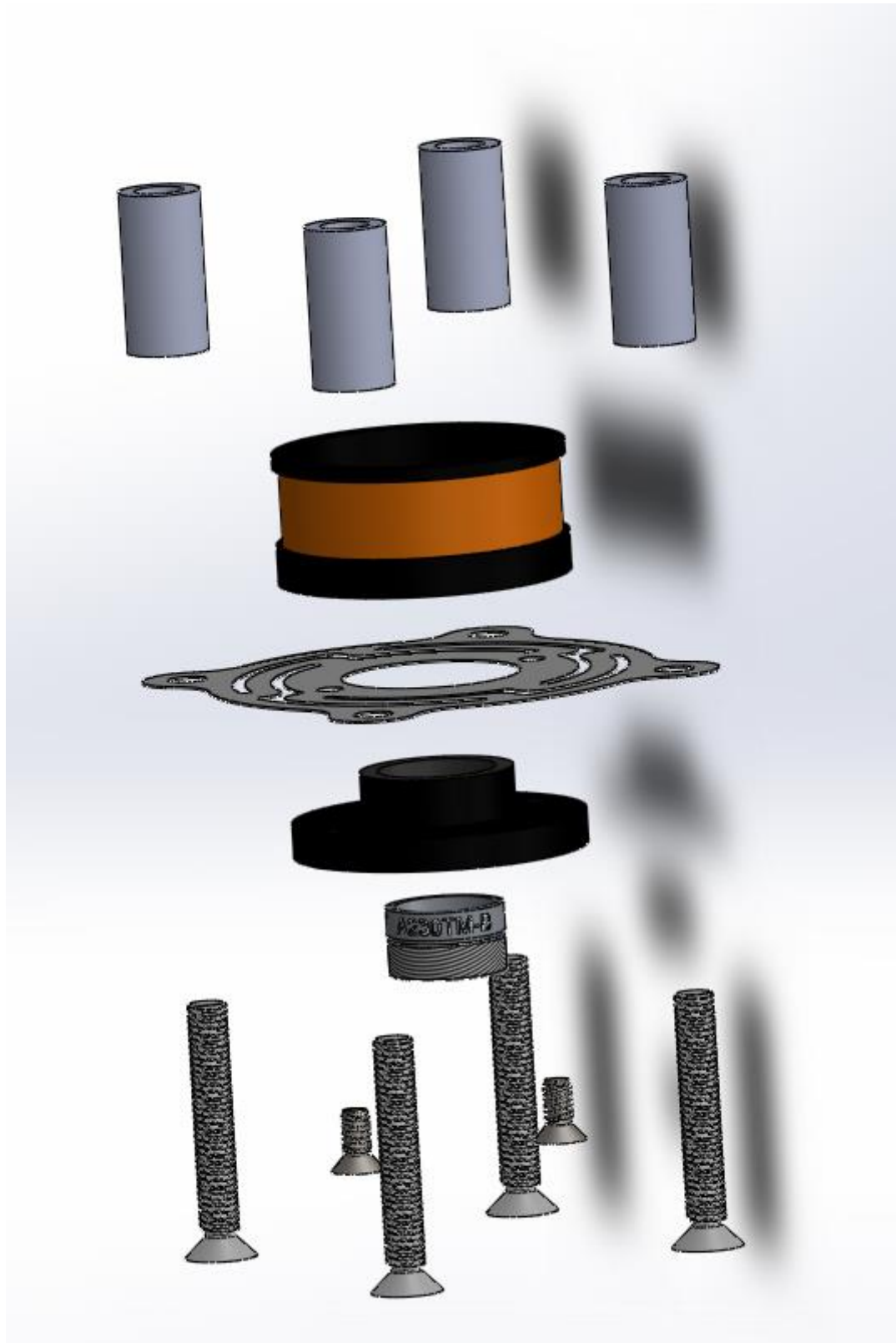






Appendix D Voice Coil Lens Actuator Assembly Details





Appendix E Operating Procedures for Imaging System

Turn-on procedure for the scanner

Step 1 Power Supply for APD

- Disconnect the power supply from the APD
- Then turn on the power supply output
- Adjust the power supply to supply +5 and -5 voltage from the +25V and -25V terminal
- Turn off the power supply output
- Connect the power supply to the APD
- Turn on the power supply output again

Step 2 Turn on NI-6363 DAQ Card

Step 3 Turn on control box for galvo mirror and resonant scanner

The galvo mirror driver will be powered and start running after turning of the control box power switch, the resonant scanner will remain inactive until the on/off switch for resonant scanner is turned on

Step 4 Turn on the laser source

- Switch the laser source control from Off to Standby
- Wait until the control board changes from one indicator light on to two indicator lights on
- Check the light path to make sure the laser is blocked in all locations and there is no laser light leaking
- Switch the laser source control from Standby to On; there should be four indicator lights on

Step 5 Open the Labview control software

Step 6 Adjust light coupling in fiber

Place the detecting probe of the light power meter in front of the scanner objective lens

Adjust the X, Y, Z direction nobs of the fiber mounting stage

Maximize the power meter reading of the light intensity

Step 7 Start imaging

For X-Y imaging, keep the current amplifier for the voice coil off and adjust the voltage outputs to control the resonant scanner and galvo mirror. Set the output amplitude for voice coil amplifier to Zero.

For X-Z imaging, set the output amplitude for galvo mirror to Zero. Turn on the current amplifier.

Turn-off procedure for the scanner

Step 1 Turn off the Labview program

Step 2 Make sure the current amplifier is turned off

Step 3 Turn off the resonant scanner switch

Step 4 Turn off the galvo mirror and resonant scanner driver control box power switch

Step 5 Turn the laser control switch from On to Standby and then to Off, no need to wait for turning off

Step 6 Turn off the NI DAQ card

